

# **Spectral correlation between surface-enhanced resonant Raman and far-field scattering destructured by dipole–quadrupole coupled plasmon resonance**

Tamitake Itoh<sup>1\*</sup>, Yuko S. Yamamoto<sup>2</sup>

<sup>1</sup>Nano-Bioanalysis Research Group, Health Research Institute, National Institute of Advanced Industrial Science and Technology (AIST), Takamatsu, Kagawa 761-0395, Japan

<sup>2</sup>School of Materials Science, Japan Advanced Institute of Science and Technology (JAIST), Nomi, Ishikawa 923-1292, Japan

\*Corresponding author: [tamitake-itou@aist.go.jp](mailto:tamitake-itou@aist.go.jp)

## **ABSTRACT**

The spectral relationships between surface-enhanced resonant Raman scattering (SERRS) and plasmon resonance observed in far-field scattering cross are investigated using single silver nanoparticle dimers with focusing on the lowest energy

(superradiant) plasmon resonance. We find that these relationships can be classified into two types. The first is SERRS spectral envelopes with spectral shapes similar to those of plasmon resonance spectra. The second is SERRS envelopes exhibiting higher energy shifts from the plasmon resonance spectra. These results are examined as an effect of degree of morphological asymmetry in dimers based on an electromagnetic (EM) mechanism. The analysis of the first and second types reveals that dipole–dipole and dipole–quadrupole coupled plasmon resonance (subradiant Fano resonance) respectively determine the EM enhancement. This mechanism is commonly important for the development of plasmonic nanostructures for various surface-enhanced spectroscopies.

## I. INTRODUCTION

Effective interaction cross-sections between light and molecules near plasmonic metal nanostructures are largely enhanced by the Purcell effect [1]. In particular, the Raman scattering of a molecule located inside a nanogap or junction of a plasmonic nanoparticle (NP) dimer exhibits an enhancement factor of up to  $10^{10}$ , enabling single-molecule Raman spectroscopy under the resonant Raman condition [2-5]. This phenomenon is called surface-enhanced resonant Raman scattering (SERRS) and its

location is called a hotspot (HS). The HSs of SERRS have received considerable attention because such locations also exhibit exotic phenomena beyond the assumptions of classical spectroscopies, e.g., strong coupling, ultrafast surface-enhanced fluorescence (ultrafast SEF), vibrational pumping, and the field gradient effect [1,6–13]. The origin of these phenomena at HSs is an extremely small plasmonic mode volume of approximately several cubic nanometers, which realizes a large amplitude in both incident light and vacuum fluctuation [1,7,8]. Thus, the relationship between these phenomena and plasmon resonance must be quantitatively clarified to control or optimize the phenomena.

The relationship between SERRS and plasmon resonance has been studied to quantitatively clarify SERRS based on an electromagnetic (EM) mechanism [14,15]. The EM mechanism describes SERRS as a product of an excitation enhancement factor  $F_R(\omega_{\text{ex}})$  and Raman scattering enhancement factor  $F_R(\omega_{\text{em}})$  by plasmon resonance as

$$F_R(\omega_{\text{ex}}, \mathbf{r})F_R(\omega_{\text{em}}, \mathbf{r}) = \left| \frac{E_{\text{loc}}(\omega_{\text{ex}}, \mathbf{r})}{E_{\text{I}}(\omega_{\text{ex}})} \right|^2 \times \left| \frac{E_{\text{loc}}(\omega_{\text{em}}, \mathbf{r})}{E_{\text{I}}(\omega_{\text{em}})} \right|^2, \quad (1)$$

where  $E_{\text{I}}$  and  $E_{\text{loc}}$  indicate the amplitudes of the incident and enhanced local electric fields, respectively;  $\omega_{\text{ex}}$  and  $\omega_{\text{em}}$  denote the frequencies of the incident and Raman-scattered light, respectively; and  $\mathbf{r}$  is the position of a molecule in a HS [4]. We

have experimentally demonstrated that SERRS spectral envelopes have shapes similar to those of plasmon resonance spectra, which are observed in far-field scattering spectra [14,15]. This spectral correlation is consistent with the EM mechanism, which predicts the spectral modulation in SERRS by  $F_R(\omega_{em})$  in Eq. (1) [15]. However, there has been controversy over the spectral correlation between SERRS and plasmon resonance. Several groups have reported SERRS spectra that are uncorrelated with plasmon resonance spectra, which were observed in far-field scattering or extinction spectra [16,17]. These reports indicate that the spectral shapes of the plasmon resonance deviate from  $F_R(\omega_{em})$  in Eq. (1). The contribution of subradiant plasmon resonance, which does not appear in far-field scattering spectra, to  $F_R(\omega_{em})$  has been discussed by several groups [18,19]. Thus, this controversy should be resolved to accurately understand the SERRS mechanism at HSs.

We examined the spectral relationships between SERRS and plasmon resonance using single silver NP dimers, focusing on the lowest energy plasmon resonance, which is the superradiant dipole resonance. The SERRS spectral envelopes were mostly similar to the plasmon resonance spectra. However, some dimers exhibited SERRS spectral envelopes that shifted to higher energy regions from the plasmon resonance maxima. There were also considerable dimer-by-dimer variations in the degree of

higher energy shifts. SERRS spectra showing the highest energy shift exhibited envelope maxima around the dips in the plasmon resonance spectra. These results were analyzed using numerical calculations based on the EM mechanism by changing the morphology of the dimers. The analysis of the calculated electric near and far fields at HSs reveals that the first type indicates that the dipole–dipole coupled plasmon resonance of symmetric dimers mainly generates EM enhancement. The second type indicates that the dipole–quadrupole coupled plasmon resonance (Fano resonance) of the asymmetric dimers dominates the EM enhancement, resulting in spectral deviation of the SERRS from plasmon resonance. These results will be useful for the development of various plasmon-enhanced spectroscopies [20].

## II. EXPERIMENT

Colloidal silver NPs (mean diameter  $\sim 35$  nm,  $1.10 \times 10^{-10}$  M) were prepared for the SERRS experiment using the Lee and Meisel method [21]. The colloidal silver NP dispersion was added to the same amount of R6G aqueous solutions ( $1.28 \times 10^{-8}$  M) with NaCl (5 mM) and left for 30 min for aggregation to obtain SERRS activity. The final concentrations of the R6G solutions ( $6.34 \times 10^{-9}$  M) and NP dispersion ( $5.5 \times 10^{-11}$  M) were within a single molecular SERRS condition, as shown by a two-analyte or isotope

technique [22,23].

The sample solution (50  $\mu\text{L}$ ) was then dropped onto a glass slide plate, and the drop was sandwiched by a glass cover plate to immobilize the SERRS-active colloidal silver NPs on the plate and left for 30 min to stably maintain the NPs on the glass slide plate. The sample plate was then set on an inverted optical microscope (IX-71; Olympus, Tokyo, Japan).

Figures 1(a1) and 1(b1) illustrate the elastic light scattering and SERRS measurements of the same sample area on a glass plate surface, respectively. Figures 1(a2) and 1(b2) are images of elastic light scattering and SERRS, respectively. The elastic scattering light of single silver NP dimers was detected by illuminating unpolarized white light from a 50-W halogen lamp through a dark-field condenser (numerical aperture (NA) 0.92). When measuring the elastic scattering light, the NA of the objective lens (LCPlanFL 100 $\times$ , Olympus, Tokyo) was set to 0.6 for dark-field illumination. The SERRS light of single silver NP dimers were measured by illuminating a circular polarized excitation green laser beam (2.33 eV (532 nm), 3.5  $\text{W}/\text{cm}^2$ ) from a CW Nd<sup>3+</sup>: YAG laser (DPSS 532, Coherent, Tokyo) on the sample plate through another objective lens (5 $\times$ , NA 0.15, Olympus, Tokyo). When measuring the SERRS light, the NA of the objective lens was increased to 1.3 to efficiently correct the

SERRS light. The elastic scattering and SERRS spectra of single NPs were measured by selecting one spot on the image plane using a pinhole in front of a polychromator equipped with a thermoelectrically cooled charge-coupled device (CCD) assembly (DV 437-OE-MCI, Andor, Japan). To measure the polarization dependence of the elastic scattering and SERRS light, both lights were detected through the polarizer. The SERRS-active silver NPs were always aggregated NPs [14]. If we selected the SERRS-active silver NP aggregates showing dipolar plasmon resonance with maxima of 1.7–2.1 eV, they were always dimers [14]. Colloidal gold NPs (mean diameters of 60, 80, and 100 nm; EMGC40, Funakoshi, Japan) were used to convert the scattering intensities to cross-sections. The detailed procedure for conversion is provided elsewhere [24].

### III. RESULTS AND DISCUSSION

We examined the variations in the spectral relationships between plasmon resonance and SERRS. Figures 2(a)–2(d) show four typical variations in the spectral relationships. Plasmon resonance appears in the elastic scattering cross-section ( $\sigma_{\text{sca}}(\omega)$ ) spectra as maxima around 1.6 to 2.0 eV of  $\hbar\omega$ , where  $\omega$  is the angular frequency of light. Figures 2(a1)–2(a4) show that the maxima of the SERRS spectral envelopes are similar to the

plasmon resonance maxima. This spectral correlation is dominant for the current SERRS-active dimers and is consistent with the EM mechanism [1,14,15]. In the EM mechanism of SERRS, the Raman process receives a two-fold enhancement from plasmon resonance, as indicated by  $F_R(\omega_{ex})$  and  $F_R(\omega_{em})$  in Eq. (1), resulting in the modulation of the SERRS spectral envelopes by  $F_R(\omega_{em})$  [14,15]. However, there are SERRS spectra that do not show such spectral similarity. Figures 2(b1)–2(b4) indicate that the SERRS spectral envelopes exhibit higher energy shifts from the plasmon resonance maxima. The degree of the higher energy shifts exhibits considerable dimer-by-dimer variations. Figures 2(c1)–2(c4) show the SERRS spectral envelopes have maxima around the dips in the  $\sigma_{sca}(\omega)$  spectra around 2.2 eV. In the case of the complex  $\sigma_{sca}(\omega)$  spectra, as indicated in Figs. 2(d1)–2(d4), were no spectral relationship was found between SERRS and  $\sigma_{sca}(\omega)$ . Thus, the dimers that showed such complex spectra were excluded from the current analysis. They may be aggregates composed of three or more NPs.

We investigated the relationship between the plasmon resonance maxima (or dips) in the  $\sigma_{sca}(\omega)$  spectra and SERRS spectral envelopes. Figure 3(a) shows the relationship between plasmon resonance maximum energy  $\hbar\omega_p$  and SERRS spectral maximum energy  $\hbar\omega_s$  for 39 dimers. Two trends are clearly observed in this relationship. One is

the proportional correlation between  $\hbar\omega_P$  and  $\hbar\omega_s$ , as indicated by the black open circles. We call this correlation “Type I.” The other is that the values of  $\hbar\omega_s$  stay around 2.1 eV; even the values of  $\hbar\omega_P$  change largely from 1.85 to 2.2 eV as indicated by the red open circles. We call this lack of correlation “Type II.” There is also an intermediate type between Types I and II, as indicated by the blue dashed circle. We further examined the relationship between the plasmon resonance dip energy  $\hbar\omega_d$  and  $\hbar\omega_s$ . Both spectral types are observed in the relationship between  $\hbar\omega_d$  and  $\hbar\omega_s$  in Fig. 3(b) as well as in Fig. 3(a). The two commonly observed spectral relationships between  $\hbar\omega_P$  (or  $\hbar\omega_d$ ) and  $\hbar\omega_s$  imply that there are two types of dimers emitting SERRS light. We consider that the dimers responsible for Type I generate EM enhancement directly via superradiant plasmon resonance. The dimers that cause Type II may generate EM enhancement via subradiant plasmon resonance and the SERRS light is emitted to free space through superradiant resonance that is coupled with the subradiant resonance [25,26]. One of the candidates of subradiant plasmons is higher-order plasmons. These higher-order plasmons, that is, quadrupole and hexapole plasmons, appear in the  $\sigma_{\text{sca}}(\omega)$  spectra of large dimers in the visible region as a result of the retardation effect [27]. Such dimers exhibit large values of  $\sigma_{\text{sca}}(\omega)$  because  $\sigma_{\text{sca}}(\omega)$  is approximately proportional to the square of the dimer volume [27]. Thus, we compared the  $\sigma_{\text{sca}}(\omega)$  at  $\hbar\omega_P$  of Type I with

those of Type II. [Figure 3\(c\)](#) shows the relationships between Types I and II. No clear differences in the distributions of Type I and II were observed, implying that the dimer size is not an important factor in causing the two different spectral trends. This result indicates that the dimer shape and not its size may be an important factor in the formation of Types I and II.

We compared the polarization dependence of the  $\sigma_{\text{sca}}(\omega)$  spectra and the SERRS intensities of dimers exhibiting Type I, the intermediate type, and Type II. [Figures 4\(a1\)–4\(c1\)](#) show the spectral relationships between  $\sigma_{\text{sca}}(\omega)$  and SERRS for Type I, the intermediate type, and Type II. The blue and black  $\sigma_{\text{sca}}(\omega)$  spectra were measured using polarization angles corresponding to the maximum and minimum  $\sigma_{\text{sca}}(\omega_{\text{P}})$ , respectively. The SERRS intensity reached a maximum at the polarization angles corresponding to the maximum  $\sigma_{\text{sca}}(\omega_{\text{P}})$ . [Figures 4\(a2\)–4\(c2\)](#) show the contour maps of the polarization dependences of the  $\sigma_{\text{sca}}(\omega)$  spectra. The superradiant plasmon resonance maxima at  $\sim 2.0$  eV exhibit a dependence on the polarization of the dipole modes. Spectral dips are observed around 2.4 eV at polarization angles yielding the maximum  $\sigma_{\text{sca}}(\omega_{\text{P}})$ . This observation indicates that the dip becomes the deepest at the polarization angle yielding the maximum  $\sigma_{\text{sca}}(\omega_{\text{P}})$ . [Figures 4\(a3\)–4\(c3\)](#) show the polarization dependence of superradiant resonance maxima and that of the averaged SERRS intensities. The

polarization dependences of the superradiant resonance maxima are identical to those of the SERRS intensities for both Types I and II. However, the depolarization rates of SERRS appear to be better than those of  $\sigma_{\text{sca}}(\omega_{\text{p}})$  for Type II. These properties are discussed in the calculation section below.

We measured the detection polarization angle  $\theta$  dependence of superradiant plasmon resonance maxima and SERRS intensities for 16 dimers to confirm the common polarization dependence for Types I and II, and the results are presented in Fig. 4. We measured the polarization angle  $\theta_{\text{Pmax}}$  of the superradiant resonance maximum and polarization angle  $\theta_{\text{Smax}}$  of the SERRS intensity maximum. We then evaluated the relationship between  $\theta_{\text{Pmax}} - \theta_{\text{Smax}}$  and  $\hbar\omega_{\text{P}} - \hbar\omega_{\text{S}}$ . The large value of  $\hbar\omega_{\text{P}} - \hbar\omega_{\text{S}}$  indicates Type II, as defined in Fig. 3(a). Figure 5(a) shows the relationship between  $\theta_{\text{Pmax}} - \theta_{\text{Smax}}$  and  $\hbar\omega_{\text{P}} - \hbar\omega_{\text{S}}$ . Their common polarization dependences not related to  $\hbar\omega_{\text{P}} - \hbar\omega_{\text{S}}$  are clearly observed, experimentally confirming the discussion of Fig. 4. Furthermore, we noticed that the depolarization rates of  $\sigma_{\text{sca}}(\omega_{\text{p}}, \theta_{\text{Pmin}})/\sigma_{\text{sca}}(\omega_{\text{p}}, \theta_{\text{Pmax}})$ , where  $\theta_{\text{Pmin}}$  is the polarization angle for the minimum of  $\sigma_{\text{sca}}(\omega_{\text{p}}, \theta)$ , are always better than  $I_{\text{S}}(\theta_{\text{Smin}})/I_{\text{S}}(\theta_{\text{Smax}})$ , where  $I_{\text{S}}$  and  $\theta_{\text{Smin}}$  are the averaged SERRS intensity and polarization angle for the minimum of  $\sigma_{\text{sca}}(\omega_{\text{p}}, \theta)$ , respectively. Figure 5(b) shows the relationship between  $\sigma_{\text{sca}}(\omega_{\text{p}}, \theta_{\text{Pmin}})/\sigma_{\text{sca}}(\omega_{\text{p}}, \theta_{\text{Pmax}})$  and  $I_{\text{S}}(\theta_{\text{Smin}})/I_{\text{S}}(\theta_{\text{Smax}})$ . For all data,

we have  $\sigma_{\text{sca}}(\omega_p, \theta_{\text{Pmin}})/\sigma_{\text{sca}}(\omega_p, \theta_{\text{Pmax}}) > I_S(\theta_{\text{Smin}})/I_S(\theta_{\text{Smax}})$ , confirming the discussion of Fig. 4.

We here discuss two SERRS processes for Types I and II based on the spectral relationships and polarization dependences. For Type I, the spectral correlation and identical polarization dependence between superradiant plasmon resonance and SERRS indicate that the SERRS signal is generated by this superradiant plasmon resonance at HS [28]. Thus, for Type I, the Raman excitation and scattering rates are increased by the superradiant resonance. In other words,  $F_R(\omega_{\text{ex}})$  and  $F_R(\omega_{\text{em}})$  in Eq. (1) are determined by superradiant resonance. For Type II, the spectral uncorrelation and identical polarization dependence between superradiant resonance and SERRS suggest that the SERRS process for Type I should be modified for Type II. Subradiant resonance may play a major role in the SERRS process for Type II, as follows. Excitation light energy is first received by superradiant resonance and then transferred to subradiant resonance, which is coupled with the superradiant resonance. Then, both the Raman excitation and scattering rates are increased by  $F_R(\omega_{\text{ex}})$  and  $F_R(\omega_{\text{em}})$  using the subradiant resonance. Finally, the generated SERRS light is emitted by the superradiant resonance through an inverse excitation process. The receiving and emitting of light by superradiant resonance may be the reason for the identical polarization dependence of superradiant

resonance and SERRS. The contribution of subradiant resonance to EM enhancement is observed as the spectral deviation of the SERRS envelopes from superradiant resonance. In other words,  $F_R(\omega_{ex})$  and  $F_R(\omega_{em})$  in Eq. (1) are determined mainly by the subradiant resonance. The intermediate type, as shown in Fig. 3(b), indicates that both superradiant and subradiant resonance contribute to the EM enhancement. The origins of superradiant and subradiant modes are discussed in the calculation section.

To clarify the abovementioned properties of the spectral and polarization relationships between superradiant plasmon resonance and SERRS, as presented in Figs. 2–5, the experimental results were analyzed by classical electromagnetism using the finite difference time domain (FDTD) method (EEM-FDM Ver.5.1, EEM Co., Ltd., Japan). The experimentally obtained properties are summarized below.

(1) There are two spectral relationships (Types I and II) between superradiant resonance and SERRS. Type I exhibits an SERRS envelope maxima in a position similar to the superradiant resonance maxima. Type II exhibits a SERRS envelope maxima of  $\sim 2.1$  eV around the dips in the  $\sigma_{sca}(\omega)$  spectra.

(2) The intermediate type between Types I and II exists continuously. In other words, SERRS envelope maxima continuously exist between the superradiant resonance maxima and dips in the  $\sigma_{sca}(\omega)$  spectra.

(3) There is no clear relationship between the values of  $\sigma_{\text{sca}}(\omega_p)$  at superradiant resonance maxima and Types I or II, indicating that dimer size is not an important factor in distinguishing Type I and II.

(4) The polarization dependences of superradiant resonance maxima and SERRS intensities are identical for both Types I and II.

The abovementioned four-fold properties were investigated using FDTD calculations. The complex refractive index of silver for NP dimers was taken from [29]. The effective refractive index of the surrounding medium was set the 1.39 from the maximum energy of gold NP with a diameter of 80 nm [24]. The validation of the calculation conditions for reproducing the experimental conditions has been described elsewhere [14,24]. Figures 6(a) and 6(b) illustrate the coordinate system of a dimer and the setup for the excitation of a dimer composed of two spherical NPs with diameters  $D_1$  and  $D_2$ , respectively, while maintaining a gap of 1 nm. We calculated the  $\sigma_{\text{sca}}(\omega)$  spectra and absorption cross-section  $\sigma_{\text{abs}}(\omega)$  spectra, as shown in Fig. 6(c), and the  $F_{\text{R}}(\omega)$  spectra with a phase of  $E_{\text{loc}}$  at the center gap, as shown in Fig. 6(d), using excitation polarization parallel to the dimer long axis. The phase of  $E_{\text{I}}$  was set to  $180^\circ$ . The  $\sigma_{\text{sca}}(\omega)$  and  $F_{\text{R}}(\omega)$  spectra obtained by unpolarized light excitation were reproduced by averaging the parallel and perpendicular excitation spectra. We define the maximum

energy in  $F_R(\omega)$  spectrum as  $\hbar\omega_F$ , which corresponds to experimentally obtained  $\hbar\omega_S$ , as indicated in Fig. 6(d).

We have discussed the origin of Types I and II shown in Fig. 3 using superradiant and subradiant plasmon resonance, respectively. The superradiant resonance generating SERRS at a HS is the dipole resonance, more correctly, the lower branch of the dipole–dipole (DD) coupled plasmon resonance of two NPs [14,15]. Here, we explore the coupled plasmon resonance arising the subradiant resonance. Figures 7(a1)–7(a10) show the diameter dependence of the  $\sigma_{\text{sca}}(\omega)$  spectra for spherical silver NPs calculated using Mie theory [27]. As the NP diameter increases, the dipole resonance in the  $\sigma_{\text{sca}}(\omega)$  spectra shifts to the lower energy region and quadrupole resonance starts to appear in the higher energy region, as shown in Fig. 7(a6), and shifts to the lower energy region, as shown in Fig. 7(a9). Figures 7(b1) and 7(b2) respectively illustrate the surface charge distribution of a dipole without a retardation effect and that of a quadrupole with a retardation effect. The appearance of dipoles and quadrupoles suggests that two types of dimer geometry candidates can arise subradiant resonance. One candidate is the dipole–quadrupole (DQ) coupled resonance of a dimer with symmetric geometry; more correctly, the lower branch of the DQ coupled plasmon resonance [18]. Figure 7(c1) illustrates the surface charge distribution of a DQ coupled plasmon of a symmetric

dimer obtained by superposing dipole and quadrupole plasmons. Such DQ coupled resonance requires spectral overlapping between the dipole and quadrupole resonances of each NP, resulting in broad resonance linewidths of the dipole plasmon, as shown in [Figs. 7\(a7\) and 7\(a9\)](#). Another candidate for subradiant resonance is the DQ coupled resonance of a dimer with asymmetric geometry. [Figure 7\(c2\)](#) illustrates the surface charge distribution of a DQ coupled plasmon of an asymmetric dimer by superposing the dipole plasmon of the smaller NP and the quadrupole plasmon of the larger NP [\[30\]](#). Such DQ coupled resonance requires a spectral overlap between the dipole resonance of the smaller NP and the quadrupole resonance of the larger NP. Thus, the combination of NPs in [Figs. 7\(a2\) and 7\(a8\)](#) can result in DQ coupled resonance when the two resonances overlap.

We examined the possibility of the DQ coupled plasmon resonance of symmetric dimers, as shown in [Fig. 7\(c1\)](#), as a subradiant plasmon resonance arising Type II. [Figures 8\(a1\)–8\(a6\)](#) show the NP diameter dependence of both the  $\sigma_{\text{sca}}(\omega)$  and  $F_{\text{R}}(\omega)$  spectra for symmetric dimers with unpolarized light excitation. The values of  $F_{\text{R}}(\omega)$  are taken from the HS, as shown in [Fig. 6\(b\)](#). As NP diameter increases, both  $\hbar\omega_{\text{p}}$  and  $\hbar\omega_{\text{F}}$  spectra exhibit lower energy shifts. During the lower energy shifts, the  $F_{\text{R}}(\omega)$  spectra broadens to the higher energy side of  $\hbar\omega_{\text{F}} \sim 2.0$  eV, as shown in [Fig. 8\(a3\)](#). Finally,  $\hbar\omega_{\text{F}}$

transfers from the position of  $\hbar\omega_P$  to the position around the dip in the  $\sigma_{\text{sca}}(\omega)$  spectrum in Fig. 8(a6) for an NP diameter of 120 nm. The dip structure is the result of destructive interference between DD and DQ coupled plasmons, indicating that the dip position corresponds to DQ coupled resonance [18]. The difference between  $\hbar\omega_P$  and  $\hbar\omega_F$  is also experimentally observed as the higher energy shifts in SERRS spectral envelopes, as shown in Fig. 3(a). These higher energy shifts in  $\hbar\omega_F$  are observed for NP diameters of 120 nm, indicating that the values of  $\sigma_{\text{sca}}(\omega_P)$  and  $\hbar\omega_P$  of DD coupled resonance for Type II dimers should be  $\gg 150 \times 10^{-3} \mu\text{m}^2$  and  $< \sim 1.6 \text{ eV}$ , respectively, as shown in Fig. 8(a6). These  $\sigma_{\text{sca}}(\omega_P)$  and  $\hbar\omega_P$  are much larger and smaller than their experimentally observed values, as shown in Fig. 3(c). Indeed, Fig. 3(c) reveals that a dimer with  $\sigma_{\text{sca}}(\omega_P)$  and  $\hbar\omega_P$  of  $\sim 5 \times 10^{-3} \mu\text{m}^2$  and 2.08 eV exhibits higher energy shifts. This large difference between the experimental and calculated values indicates that the symmetric dimer may not be a candidate for Type II.

Next, the DQ coupled plasmon resonance of the asymmetric dimers, as shown in Fig. 7(c2), was evaluated as a candidate of Type II. Figures 8(b1)–8(b6) show the  $D_1$  dependence of both the  $\sigma_{\text{sca}}(\omega)$  and  $F_R(\omega)$  spectra at the HS while fixing  $D_2$  at 30 nm using unpolarized light excitation. As  $D_1$  increases, both  $\hbar\omega_P$  and  $\hbar\omega_F$  exhibit lower energy shifts until  $D_1$  reaches 80 nm, as shown in Figs. 8(b1)–8(b3). For  $D_1 > 80 \text{ nm}$ ,

$\hbar\omega_p$  exhibits further lower energy shifts, but  $\hbar\omega_F$  remains at approximately 2.2 eV, as shown in Figs. 8(b3)–8(b5). Finally,  $\hbar\omega_F$  overlaps with the dip position in the  $\sigma_{\text{sca}}(\omega)$  spectrum, which may be the DQ coupled resonance position, as shown in Fig. 8(b6), for a  $D_1$  of 120 nm. This difference in trends between  $\hbar\omega_p$  and  $\hbar\omega_F$  is consistent with the experimentally observed higher energy shifts in the SERRS spectra, as shown in Figs. 2(b) and 2(c). Furthermore, the values of the calculated  $\sigma_{\text{sca}}(\omega)$  and  $\hbar\omega_p$  are reasonably consistent with the experimental ones for Type II, as shown in Fig. 3(c). Thus, we consider that the asymmetry in the dimers causes DQ coupled resonance, resulting in Type II. In short, the subradiant resonance discussed in the experimental section is the DQ coupled resonance of the asymmetric dimers.

Figure 8 indicates that asymmetric dimers cause the spectral deviation in the DD coupled plasmon resonance from the SERRS envelope based on the spectral relationships between the DQ (or DD) coupled resonance and  $F_R(\omega)$  at HSs. To confirm this indication, we provide evidence of DQ (or DD) coupled resonance observed in the  $\sigma_{\text{sca}}(\omega)$  and  $F_R(\omega)$  spectra. The evidence is the amount of phase retardation of  $E_{\text{loc}}$  against the phase of  $E_I$ . The  $E_{\text{loc}}$  of the DD coupled resonance induces a phase retardation of  $90^\circ$  from  $E_I$  [1]. The phase of  $E_{\text{loc}}$  of the DQ coupled resonance obtains a further retardation of  $90^\circ$  from the DD coupled resonance because the DQ coupled

resonance receives light energy by coupling with the DD coupled resonance [25,26].

Thus, the  $E_{\text{loc}}$  of DQ coupled resonance exhibits a phase retardation of  $180^\circ$  from  $E_{\text{I}}$ .

The destructive interference between the  $E_{\text{loc}}$  of DD coupled resonance and the  $E_{\text{loc}}$  of DQ coupled resonance appears as a dip structure in the  $\sigma_{\text{sca}}(\omega)$  spectrum.

We calculated the relationship between the DD (or DQ) resonance and the phase of  $E_{\text{loc}}$  with an excitation polarization parallel to the dimer long axis. Figures 9(a1)–9(a4) show the  $D_1$  dependence of  $\sigma_{\text{sca}}(\omega)$  and  $\sigma_{\text{abs}}(\omega)$  spectra on the phases of  $E_{\text{loc}}$ . The initial phase of  $E_{\text{I}}$  was set to  $180^\circ$  and  $D_2$  was set to 30 nm. Both  $\sigma_{\text{sca}}(\omega)$  and  $\sigma_{\text{abs}}(\omega)$  spectra exhibit a phase retardation of  $E_{\text{loc}}$  of  $90^\circ$  at  $\hbar\omega_{\text{p}}$ , indicating that these spectral maxima correspond to DD coupled resonance. With increasing  $D_1$ , the DD coupled resonance spectra becomes broader because of the increasing effect of radiation damping [31]. The values of  $\sigma_{\text{abs}}(\omega)$  become smaller than  $\sigma_{\text{sca}}(\omega)$ , because  $\sigma_{\text{sca}}(\omega)$  and  $\sigma_{\text{abs}}(\omega)$  are proportional to the square of and linear with respect to dimer volume, respectively [27]. As  $D_1$  increases further, the dip structure clearly appears in the  $\sigma_{\text{sca}}(\omega)$  spectrum at a phase retardation of  $180^\circ$ , indicating that the spectral dip is the result of destructive interference between the DD and DQ coupled resonance.

Figures 9(b1)–9(b4) show the  $D_1$  dependence of  $F_{\text{R}}(\omega)$  spectra at a HS with the phase of  $E_{\text{loc}}$ . The  $F_{\text{R}}(\omega)$  spectrum in Fig. 9(b1) exhibits  $\hbar\omega_{\text{F}}$  at a phase retardation of  $90^\circ$ ,

indicating that the maximum is the result of EM enhancement by the DD coupled resonance. As  $D_1$  increased,  $\hbar\omega_F$  exhibits a lower energy shift, as shown in Figs. 9(b2). However, the lower energy shift in  $\hbar\omega_F$  does not occur in Figs. 9(b3) and  $\hbar\omega_F$  remains at approximately  $\sim 2.18$  eV, as shown in Fig. 9(b4), where the phase retardation is  $180^\circ$ . This position is the same as the dip in the  $\sigma_{\text{sca}}(\omega)$  spectrum shown in Fig. 9(a4), indicating that the  $F_R(\omega)$  maximum at  $\hbar\omega_F$  is the result of EM enhancement by the DQ coupled resonance, which obtains light energy through DD coupled resonance. This mechanism of EM enhancement by the DQ coupled resonance explains the experimentally observed higher energy shifts in SERRS envelope maxima well, as shown in Figs 2(b) and 2(c). This mechanism also explains the reason the SERRS envelope maximum positions matches the dip positions in the  $\sigma_{\text{sca}}(\omega)$  spectra in Figs. 2(b) and 2(c).

DQ coupled resonance obtains light energy through near-field interactions between DD and DQ coupled resonance. Moreover, the main portion of the obtained light energy is dissipated as thermal energy. Thus, the  $F_R(\omega)$  spectra should be correlated with the  $\sigma_{\text{abs}}(\omega)$  spectra rather than the  $\sigma_{\text{sca}}(\omega)$  spectra. Figures 9(c1)–9(c4) show the  $D_1$  dependence of the  $\sigma_{\text{abs}}(\omega)$  and  $F_R(\omega)$  spectra. As expected, the  $F_R(\omega)$  maxima are well correlated with the spectral maxima of  $\sigma_{\text{abs}}(\omega)$ , indicating that subradiant resonance

such as DQ coupled resonance should be observed by absorption spectroscopy. This also indicates that the broad background emission spectra of the SERRS, which is an ultrafast SEF [10,11], can be used to measure such subradiant resonance spectra.

In short, the experimentally observed spectral deviation of the SERRS envelopes from DD coupled resonance is explained as the contribution of DQ coupled resonance, which is the subradiant resonance, to the EM enhancement. Figure 9 summarizes the spectral relationships between  $\sigma_{\text{sca}}(\omega)$ ,  $\sigma_{\text{abs}}(\omega)$ ,  $F_{\text{R}}(\omega)$ , and the phase of  $E_{\text{loc}}$  at the HSs for asymmetric dimers to clarify the mechanism of this spectral deviation.

We visualized the relationships between the NP diameter,  $\sigma_{\text{sca}}(\omega)$ ,  $\sigma_{\text{abs}}(\omega)$ ,  $F_{\text{R}}(\omega)$ , and the phase of  $E_{\text{loc}}$  at the HSs to understand the switching mechanism of the EM enhancement from DD to DQ coupled resonance. Figures 10(a1)–10(a4) show the NP diameter dependence of the spectra of  $\sigma_{\text{sca}}(\omega)$ ,  $\sigma_{\text{abs}}(\omega)$ ,  $F_{\text{R}}(\omega)$ , and the phase of  $E_{\text{loc}}$  at the HSs, respectively, for symmetric dimers using contour maps. The photon energies at phase retardations of  $90^\circ$  and  $180^\circ$  are shown as inserts in Figs. 10(a1)–10(a4) to indicate the positions of DD and DQ coupled resonance. In the  $\sigma_{\text{sca}}(\omega)$  spectra in Fig. 10(a1), both resonances show lower energy shifts with increasing NP diameter, and the DQ coupled resonance always appears as a dip structure. In the  $\sigma_{\text{abs}}(\omega)$  spectra in Fig. 10(a2), both resonances also show lower energy shifts with increasing NP diameter.

However, the appearance of DQ coupled resonance changes from a dip to a peak structure for NP diameters  $>120$  nm. This change is due to the light energy transfer from DD to DQ coupled resonance by when their spectra overlap because of the broadening of the DD coupled resonance. In the  $F_R(\omega)$  spectra in Fig. 10(a3), the behaviors of both resonances are similar to those observed in the  $\sigma_{\text{abs}}(\omega)$  spectra, indicating that  $\sigma_{\text{abs}}(\omega)$  spectra are always correlated to  $F_R(\omega)$ , generating SERRS.

Figures 10(b1)–10(b4) show the  $D_1$  dependence of the spectra of  $\sigma_{\text{sca}}(\omega)$ ,  $\sigma_{\text{abs}}(\omega)$ , and  $F_R(\omega)$  as well as the phase of  $E_{\text{loc}}$  at the HSs for asymmetric dimers while keeping  $D_2$  at 30 nm. The phase retardations of  $E_{\text{loc}}$  of  $90^\circ$  and  $180^\circ$  are shown as inserts in Figs. 10(b1)–10(b3). In the  $\sigma_{\text{sca}}(\omega)$  spectra in Fig. 10(b1), both resonances shift to the lower energy region as  $D_1$  increases, and DQ coupled resonance always appear as a dip structure. In the  $\sigma_{\text{abs}}(\omega)$  spectra in Fig. 10(b2), the absorption peak at 2.25 eV first follows the DD coupled resonance until  $D_1$  reaches approximately 80–100 nm and then gradually switches to the DQ coupled resonance at 2.15 eV as  $D_1$  further increases. The switch behavior is induced by the energy transfer from DD coupled resonance to DQ coupled resonance with their near-field interaction. This analysis of the spectra of  $\sigma_{\text{sca}}(\omega)$ ,  $\sigma_{\text{abs}}(\omega)$ , and  $F_R(\omega)$  along with the phase of  $E_{\text{loc}}$  at the HSs for asymmetric dimers clarifies the experimentally observed spectral deviation of SERRS envelopes

from the DD coupled resonance. This deviation is induced by excitation light energy transfer from the DD to the DQ coupled resonance when their spectra overlap.

We compared the experimental and calculated results to examine the mechanism of the spectral deviation in the SERRS envelopes caused by superradiant plasmon resonance in  $\sigma_{\text{sca}}(\omega)$ . [Figure 11\(a\)](#) shows the calculated relationship between  $\hbar\omega_{\text{p}}$  in the  $\sigma_{\text{sca}}(\omega)$  spectra and  $\hbar\omega_{\text{F}}$  in the  $F_{\text{R}}(\omega)$  spectra. This relationship is superposed with the experimentally obtained relationship between  $\hbar\omega_{\text{p}}$  and  $\hbar\omega_{\text{S}}$  shown in [Fig. 3\(a\)](#). The calculated relationship reproduces both Type I and II well using the symmetric and asymmetric dimers, respectively, indicating the validity of the mechanism in which Types I and II are raised by DD and DQ coupled resonance, respectively. [Figure 11\(b\)](#) shows the calculated relationship between  $\hbar\omega_{\text{d}}$  in the  $\sigma_{\text{sca}}(\omega)$  spectra and  $\hbar\omega_{\text{F}}$  in the  $F_{\text{R}}(\omega)$  spectra. This relationship is superimposed with the experimental relationship between  $\hbar\omega_{\text{d}}$  and  $\hbar\omega_{\text{S}}$  in [Fig. 3\(b\)](#). The calculated relationship also reproduces Types I and II, further supporting the validity of the mechanism generating Types I and II. The dimer of Type II generates SERRS using DQ coupled resonance, and SERRS light is transmitted to free space by the DD coupled resonance. [Figure 11\(c\)](#) presents the relationship between  $\hbar\omega_{\text{p}}$  and  $\sigma_{\text{sca}}(\omega)$  at  $\hbar\omega_{\text{p}}$ . This relationship is superimposed with the experimental relationship between  $\hbar\omega_{\text{p}}$  at  $\sigma_{\text{sca}}(\omega)$  in [Fig. 3\(c\)](#). Both the calculation and

experimental results show the common trend of the increase in  $\sigma_{\text{sca}}(\omega_{\text{P}})$  causing lower energy shifts in  $\hbar\omega_{\text{P}}$ . The calculated distribution of data for the symmetric dimers is not separated from those for the asymmetric dimers, supporting the experimental data. However, the calculated values  $\sigma_{\text{sca}}(\omega_{\text{P}})$  are always larger than the experimental values, indicating that the experimental NPs deviated from the spherical shapes. The discussion of Fig. 11 explains the experimentally obtained properties (1)–(3) well as the SERRS properties of symmetric and asymmetric dimers.

In Fig. 4, we experimentally observed property (4): the common polarization dependence between superradiant plasmon resonance and SERRS for both Types I and II. This property was also verified by 15 dimers, as shown in Fig. 5(a). Furthermore, two additional properties were found in the polarization dependence. (I) The spectral dip in  $\sigma_{\text{sca}}(\omega)$  becomes deepest at the same polarization angles as those of the spectral maxima for superradiant resonance. (II) The depolarization ratios of the SERRS are much better than those of superradiant plasmon resonance. This property was also verified by the 15 dimers in Fig. 5(b). These properties are here examined by calculating  $\sigma_{\text{sca}}(\omega)$  and  $F_{\text{R}}(\omega)$  using asymmetric dimers.

Property (4) can be rephrased as the common polarization dependence of DD coupled resonance and  $F_{\text{R}}(\omega)$ , which is generated by DD coupled resonance (Type I) or by DQ

coupled resonance (Type II). Property (I) appears obvious because both DD and DQ coupled resonance have the same polarization dependence with respect to the charge distribution in Fig. 7(c2). We verified property (I) by calculating the asymmetric dimers. Figures 12(a1)–12(a4) and 12(b1)–12(b4) show the polarization dependence of the  $\sigma_{\text{sca}}(\omega)$  and  $F_{\text{R}}(\omega)$  spectra, respectively, by increasing  $D_1$  while keeping  $D_2$  fixed at 30 nm. For excitation light that is polarized parallel to the dimer long axis, both  $\sigma_{\text{sca}}(\omega)$  and  $F_{\text{R}}(\omega)$  exhibit spectral changes with increasing  $D_1$ , as already illustrated in Fig. 9(a) and Fig. 9(b), respectively. For excitation polarization that is perpendicular to the dimer long axis, the dipole resonance in  $\sigma_{\text{sca}}(\omega)$  exhibits a lower energy shifts with broadening, and  $F_{\text{R}}(\omega)$  becomes negligible because this dipole resonance cannot generate EM enhancement inside a HS [14]. The common polarization dependences of DD coupled resonance and  $F_{\text{R}}(\omega)$  for both Type I (Figs. 12(a1) and 12(b1)) and Type II (Figs. 12(a4) and 12(b4)) are clearly reproduced in the calculations.

Property (I) can be rephrased as follows: the DQ coupled resonance appears as the deepest dip at the same polarization angles as the maxima of DD coupled resonance. Property (II) also appears obvious because both DD and DQ coupled resonance have the same polarization dependence with respect to the charge distribution in Fig. 7(c2). We verified property (II) using calculation. To reproduce Figs. 4(a2)–4(c2), the polarization

dependences of  $\sigma_{\text{sca}}(\omega)$  are expressed as contour maps by increasing  $D_1$  while keeping  $D_2$  fixed at 30 nm, as shown in Figs. 12(c1)–12(c4). The contour maps were created by superposing both contour maps of parallel and perpendicular excitation with respect to the unpolarized excitation condition. As  $D_1$  increases, the dip structure due to DQ coupled resonance appears in the higher energy side of the DD coupled resonance, and the dip becomes the deepest at the same polarization angles of the maxima of the DD coupled resonance, as shown in Figs. 12(c3) and 12(c4). These structures are consistent with the experimentally observed polarization dependence, as shown in Figs. 4(a2)–4(c2). This calculation indicates that the light energy transfer from DD to DQ coupled resonance becomes the most efficient at the polarization angles of the maxima of the DD coupled resonance, resulting in the deepest dip in the  $\sigma_{\text{sca}}(\omega)$  spectra.

Property (II) can be rephrased as the fact that the depolarization ratio of  $F_{\text{R}}(\omega_{\text{F}})$  is better than the depolarization ratio of  $\sigma_{\text{sca}}(\omega_{\text{p}})$ . By comparing Figs. 12(a1)–12(a4) and Figs. 12(b1)–12(b4), one can notice that the depolarization ratios of  $F_{\text{R}}(\omega)$ s at  $\hbar\omega_{\text{F}}$  are much better than those of  $\sigma_{\text{sca}}(\omega)$  at  $\hbar\omega_{\text{p}}$ . Figures 12(d1)–12(d4) show the polarization dependence of  $\sigma_{\text{sca}}(\omega_{\text{p}})$  and  $F_{\text{R}}(\omega_{\text{F}})$  with increasing  $D_1$ . The depolarization ratios of  $F_{\text{R}}(\omega)$  become better than those of  $\sigma_{\text{sca}}(\omega)$  with increasing  $D_1$ . The results are consistent with experiments, indicating the reason for the better depolarization ratio of  $F_{\text{R}}(\omega)$  is as

follows.  $F_R(\omega)$  is solely generated by DD or DQ coupled resonance polarized in the direction parallel to the dimer long axis. In contrast,  $\sigma_{\text{sca}}(\omega)$  includes spectral components both parallel and perpendicular to the long axis of the dimer. Thus, the depolarization ratios of  $\sigma_{\text{sca}}(\omega)$  degrade because of the inclusion of scattering light from the dipole resonance polarized perpendicular to the dimer long axis, as shown in [Fig. 12\(a4\)](#).

In the experiments using 15 dimers shown in [Fig. 5](#), we evaluated property (4), which is the common polarization dependence for superradiant plasmon resonance and SERRS for both Type I and II. We also confirmed property (I) for the symmetric and asymmetric dimers by changing both  $D_1$  and  $D_2$  by calculation. [Figure 13](#) shows that all dimers for both Types I and II exhibit common polarization angle dependences for  $\sigma_{\text{sca}}(\omega_P)$  and  $F_R(\omega_F)$ , which reproduces the experimental results in [Fig. 5](#).

We discussed the spectral and polarization properties of SERRS based on DD or DQ coupled resonance. The two types of spectral relationships between SERRS and  $\sigma_{\text{sca}}(\omega)$ , Types I and II, are well explained as the presence and absence of the contribution of DQ coupled resonance to SERRS, respectively. Here, we examined the radiation patterns of dimers of Type II to confirm the contribution of DQ coupled resonance to SERRS radiation. The dimers of Type I have symmetric structures and SERRS is generated by

DD coupled resonance. Thus, the radiation pattern from the HSs exhibits dipole properties. By contrast, the dimers of Type II have asymmetric structures and their SERRS is generated by DQ coupled resonance. Thus, the radiation pattern from the HSs may deviate from the dipolar property, reflecting the destructive interference between DD and DQ coupled resonance.

Figure 14(a) shows the spectra of  $\sigma_{\text{sca}}(\omega)$  and  $F_{\text{R}}(\omega)$ , and the phase of  $E_{\text{loc}}$  at HSs for an asymmetric dimer, which is an intermediate type between Type I and II. The position of  $\hbar\omega_{\text{F}}$  is located between a phase retardation of  $90^\circ$  and  $180^\circ$ . We analyzed the charge distributions and radiation patterns for phase retardations of  $90^\circ$ ,  $180^\circ$ , and  $270^\circ$ , as respectively indicated by three black lines corresponding to DD, DQ, and DD coupled resonance. Figures 14(b1)–14(b3) illustrate the charge distributions in the z-plane for DD, DQ, and DD coupled plasmons at the three spectral positions in Fig. 14 (a). The charge distributions of the DD coupled plasmons in Figs. 14(b1) and 14(b3) indicate that the dimer exhibits a dipole radiation pattern. Figure 14(b2) illustrates the charge distribution of DQ coupled plasmons. Referring to the generalized Kerker effect on the electric dipole and quadrupole [32], this charge distribution indicates destructive interference of the radiation field between the quadrupole and dipole when the radiation is directed toward the larger NP side. In addition, constructive interference occurs when

the radiation is directed toward the smaller NP side. Such destructive and constructive interference bends the dipole-like radiation, as shown in Fig. 14(c). This radiation pattern of DQ coupled resonance has been reported in plasmon-enhanced second-harmonic generation [33-35]. We calculated the near electric fields around the dimer to examine the radiation patterns for each phase retardation. Figures 14(d1)–14(d3) show cross-sectional images (y-planes) of the distributions of  $E_{loc}$  for each phase radiation. These  $E_{loc}$  distributions appear complex, but  $E_{loc}$  in Fig. 14(d2) shows the bending in the distribution in the direction of the smaller NP, as indicated by the green arrows. This property is consistent with the radiation pattern of DQ coupled resonance in Fig. 14(c). We also examined the far-field radiation patterns of each spectral position. Figures 14(e1)–14(e3) show the polar diagram of the radiation patterns for DD, DQ, and DD coupled resonance. The radiation patterns in Figs. 14(e1) and 14(e3) exhibit dipole features. However, Figs. 14(e2) shows bending to the side of the smaller NP. Such bending is evidence of the contribution of DQ coupled resonance to the radiation pattern.

In Fig. 10, we observe that  $F_R(\omega)$  is dominated by DQ coupled plasmons by increasing the degree of asymmetry in the dimer structures. The degree of asymmetry also affects the far-field radiation pattern as it deviates from the dipolar radiation pattern.

Thus, the contribution of DQ coupled resonance to SERRS can be evaluated by polar diagrams as the bending of the radiation direction, as shown in Figs. 14(e2). Thus, we examined the bending angles of the radiation patterns by changing the degree of asymmetry, which is defined as  $D_1/D_2$ , as shown in Fig. 6(b). Figure 15 shows the relationship between  $D_1/D_2$  and the bending angle  $\phi$ , which is defined in the inset of Fig. 15. In symmetric dimers, the values of  $\phi$  are always  $0^\circ$ . Increasing  $D_1/D_2$  causes  $\phi$  to increase and saturate at  $\sim 35^\circ$ . This bending, which can be experimentally observed using a Fourier imaging method [36,37], is useful for evaluating the contribution of DQ coupled resonance to SERRS.

#### IV. SUMMARY

We investigated Type I and II spectral relationships between SERRS and superradiant plasmon resonance in  $\sigma_{\text{sca}}(\omega)$  using a single silver NP dimer. Type I shows SERRS envelopes that are similar to plasmon resonance maxima. Type II exhibits SERRS envelopes that shift the higher energy side from the plasmon resonance maxima. The FDTD calculation, by changing the degree of morphological asymmetry in the dimers, reproduced the experimental spectra and polarization properties well for both  $\sigma_{\text{sca}}(\omega)$  and SERRS. The analysis of the calculation results revealed that Types I and II are

raised by DD and DQ coupled resonance, respectively. DQ coupled resonance, which is subradiant, receives excitation light and emits SERRS light through near-field interaction with DD coupled resonance. The contribution of DQ coupled resonance to SERRS was also evaluated using the deviation of the radiation pattern from that of a dipole. This study contributes to the evaluation of the EM enhancement of various plasmonic HSs composed of NP or nanowire dimers, NPs on mirrors, and NP clusters [14,38-41].

## ACKNOWLEDGMENTS

This work was supported by a JSPS KAKENHI Grant-in-Aid for Scientific Research (C), number 21K04935.

## REFERENCES

- [1] T. Itoh, Y. S. Yamamoto, and Y. Ozaki, *Chem. Soc. Rev.* **46**, 3904 (2017).
- [2] S. Nie and S. Emory, *Science* **275**, 1102 (1997).
- [3] K. Kneipp, Y. Wang, H. Kneipp, L. Perelman, I. Itzkan, R. R. Dasari, and M. Feld, *Phys. Rev. Lett.* **78**, 1667 (1997).
- [4] H. Xu, E. J. Bjerneld, M. Käll, and L. Börjesson, *Phys. Rev. Lett.* **83**, 4357 (1999).

- [5] A. M. Michaels, M. Nirmal, and L. E. Brus, *J. Am. Chem. Soc.* **121**, 9932 (1999).
- [6] Y. S. Yamamoto, Y. Ozaki, and T. Itoh, *J. Photochem. Photobio. C* **21**, 81 (2014).
- [7] J. J. Baumberg, J. Aizpurua, M. H. Mikkelsen, and D. R. Smith, *Nat. Mater.* **18**, 668 (2019).
- [8] T. Itoh and Y. S. Yamamoto, *Nanoscale* **13**, 1566 (2021).
- [9] Itoh, Y. S. Yamamoto, H. Tamaru, V. Biju, S. Wakida, and Y. Ozaki, *Phys. Rev. B* **89**, 195436 (2014).
- [10] E. C. Le Ru, P. G. Etchegoin, J. Grand, N. Félidj, J. Aubard, and G. Lévi, *J. Phys. Chem. C* **111**, 44, 16076–16079 (2007).
- [11] T. Itoh, Y. S. Yamamoto, H. Tamaru, V. Biju, N. Murase, and Y. Ozaki, *Phys. Rev. B* **87**, 235408 (2013).
- [12] K. Kneipp, Y. Wang, H. Kneipp, Ir. Itzkan, R. R. Dasari, and M. S. Feld, *Phys. Rev. Lett.* **76**, 2444 (1996).
- [13] F. Benz, M. K. Schmidt, A. Dreismann, R. Chikkaraddy, Y. Zhang, A. Demetriadou, C. Carnegie, H. Ohadi, B. de Nijs, R. Esteban, J. Aizpurua, and J. J. Baumberg, *Science* **354**, 726 (2016).
- [14] K. Yoshida, T. Itoh, H. Tamaru, V. Biju, M. Ishikawa, and Y. Ozaki, *Phys. Rev. B* **81**, 115406 (2010).

- [15] T. Itoh, M. Iga, H. Tamaru, K. Yoshida, V. Biju, and M. Ishikawa, *J. Chem. Phys.* **136**, 024703 (2012).
- [16] M. D. Doherty, A. Murphy, R. J. Pollard, and P. Dawson, *Phys. Rev. X* **3**, 011001 (2013)
- [17] S. L. Kleinman, B. Sharma, M. G. Blaber, A.-I. Henry, N. Valley, R. G. Freeman, M. J. Natan, G. C. Schatz, and R. P. Van Duyne, *J. Am. Chem. Soc.* **135**, 301–308 (2013).
- [18] Y. Tanaka, A. Sanada, and K. Sasaki, *Sci. Rep.* **2**, 764 (2012).
- [19] J. Ye, F. Wen, H. Sobhani, J. B. Lassiter, P. Van Dorpe, P. Nordlander, and N. J. Halas, *Nano Lett.* **12**, 1660–1667 (2012).
- [20] J. Langer, et al., *ACS Nano* **14**, 28-117 (2020).
- [21] P. Lee and D. Meisel, *J. Phys. Chem.* **86**, 3391 (1982).
- [22] E. C. Le Ru, M. Meyer, and P. G. Etchegoin, *J. Phys. Chem. B* **110**, 1944 (2006).
- [23] A. B. Zrimsek, A. I. Henry, and R. P. Van Duyne, *J. Phys. Chem. Lett.* **4**, 3206 (2013).
- [24] T. Itoh, Y. S. Yamamoto, and T. Okamoto, *Phys. Rev. B*, **99**, 235409 (2019).
- [25] J. A. Fan, C. Wu, K. Bao, J. Bao, R. Bardhan, N. J. Halas, V. N. Manoharan, P. Nordlander, G. Shvets, and F. Capasso, *Science* **328**, 1135 (2010)

- [26] Z. J. Yang, Z. S. Zhang, L. H. Zhang, Q. Q. Li, Z. H. Hao, and Q. Q. Wang, *Opt. Lett.* **36**,1542, (2011).
- [27] C. F. Bohren and D. R. Huffman, *Absorption and Scattering of Light by Small Particles* (Wiley, New York, 1983).
- [28] T. Itoh and Y. S. Yamamoto, *J. Chem. Phys.* **149**, 244701 (2018).
- [29] P. B. Johnson and R. W. Christy, *Phys. Rev. B* **6**, 4370–4379 (1972).
- [30] L. V. Brown, H. Sobhani, J. B. Lassiter, P. Nordlander, and N. J. Halas, *ACS Nano* **4**, 819–832 (2010).
- [31] C. Sönnichsen, T. Franzl, T. Wilk, G. von Plessen, J. Feldmann, O. Wilson, and P. Mulvaney, *Phys. Rev. Lett.* **88**, 077402 (2002).
- [32] W. Liu and Y. S. Kivshar, *Opt. Express* **26**, 13085–13105 (2018).
- [33] J. I. Dadap, J. Shan, K. B. Eisenthal, and T. F. Heinz, *Phys. Rev. Lett.* **83**, 4045 (1999).
- [34] J. Butet, G. D. Bernasconi, M. Petit, A. Bouhelier, C. Yan, Olivier, J. F. Martin, B. Cluzel, and O. Demichel, *ACS Photonics* **4**, 11, 2923–2929, (2017).
- [35] K. Guo, Y. L. Zhang, C. Qian, and K. H. Fung, *Opt. Express* **26**, 11984–11993, (2018).
- [36] T. Shegai, V. D. Miljkovic, K. Bao, H. Xu, P. Nordlander, P. Johansson, and M.

Kall, *Nano Lett.* **11**, 706–711 (2011).

[37] M. P. Backlund, M. D. Lew, A. S. Backer, S. J. Sahl, and W. E. Moerner, *ChemPhysChem* **15**, 587–599, (2014).

[38] T. Itoh, T. Y. S. Yamamoto, Y. Kitahama, and J. Balachandran, *Phys. Rev. B* **95**, 115441 (2017).

[39] T. Itoh, T. Y. S. Yamamoto, and J. Balachandran, *Phys. Rev. B* **103**, 245425 (2021).

[40] C. Ciraci, R. T. Hill, J. J. Mock, Y. Urzhumov, A. I. Fernandez-Dominguez, S. A. Maier, J. B. Pendry, A. Chilkoti, and D. R. Smith, *Science* **337**, 1072–1074 (2012).

[41] S. Y. Ding, E. M. You, Z. Q. Tian, and M. Moskovits, *Chem. Soc. Rev.* **46**, 4042–4076 (2017).

## Figure captions

**FIG. 1 (a1)** Dark-field illumination of a silver NP dimer. The dimer placed on the cover glass is excited from above and forward elastic scattered light is detected. The polarization dependence of the scattered light is measured by rotating the polarizer. **(a2)** Dark-field image of NPs and NP aggregates on the cover glass. The single light spot is selected by a pinhole to measure the elastic scattering spectra of a single dimer. The

scale bar is 5  $\mu\text{m}$ . (b1) SERRS excitation of a NP dimer. The dimer is excited from above and forward SERRS light is detected. The polarization dependence of the SERRS light is measured by rotating the common polarizer. (b2) SERRS image of NP aggregates on the cover glass. The scale bar is 5  $\mu\text{m}$ .

FIG. 2 (a1)–(a4)  $\sigma_{\text{sca}}(\omega)$  spectra (blue lines) and SERRS spectra (red lines) of single dimers exhibiting similar spectral shapes (Type I). (b1)–(b4)  $\sigma_{\text{sca}}(\omega)$  spectra and SERRS spectra of single dimers exhibiting spectral deviation with respect to each other (intermediate type). (c1)–(c4)  $\sigma_{\text{sca}}(\omega)$  spectra and SERRS spectra with maxima that are close to spectral dips in the elastic scattering (Type II). (d1)–(d4)  $\sigma_{\text{sca}}(\omega)$  spectra and SERRS spectra for large aggregates.

FIG. 3 (a) Relationship between the  $\hbar\omega_p$  and  $\hbar\omega_s$  of single dimers exhibiting Type I (black circles) and Type II (red circles). The data of the intermediate type are surrounded by a dashed blue circle. (b) Relationship between the  $\hbar\omega_d$  and  $\hbar\omega_s$  of single dimers exhibiting Type I (black circles) and Type II (red circles). (c) Relationship between the  $\hbar\omega_p$  and  $\sigma_{\text{sca}}(\omega_p)$  of single dimers exhibiting Type I (black circles) and Type II (red circles).

**FIG. 4 (a1)–(c1)**  $\sigma_{\text{sca}}(\omega)$  spectra (blue and black curves) and SERRS spectra (red curves) of single dimers exhibiting Type I **(a1)**, intermediate type **(b1)**, and Type II **(c1)** with unpolarized excitation. The blue and black  $\sigma_{\text{sca}}(\omega)$  spectra were measured with polarization angles with the maximum and minimum  $\sigma_{\text{sca}}(\omega_{\text{p}})$ , respectively. **(a2)–(c2)** Detection polarization angle dependence of the  $\sigma_{\text{sca}}(\omega)$  spectra of single dimers exhibiting Type I **(a2)**, intermediate type **(b2)**, and Type II **(c2)** with unpolarized excitation. The spectral maxima and dips are indicated by solid and dashed circles, respectively. **(a3)–(c3)** Detection polarization angle dependence of  $\sigma_{\text{sca}}(\omega_{\text{p}})$  and SERRS intensity of single dimers exhibiting Type I **(a3)**, intermediate type **(b3)**, and Type II **(c3)** with unpolarized excitation.

**FIG. 5 (a)** Relationship between the  $\theta_{\text{Pmax}} - \theta_{\text{Smax}}$  and  $\hbar\omega_{\text{p}} - \hbar\omega_{\text{S}}$  of single dimers. The degrees of Types I and II are indicated by the black and red colored arrow. **(b)** Relationship between the  $\sigma_{\text{sca}}(\omega_{\text{p}}, \theta_{\text{Pmin}})/\sigma_{\text{sca}}(\omega_{\text{p}}, \theta_{\text{Pmax}})$  and  $I_{\text{S}}(\theta_{\text{Smin}})/I_{\text{S}}(\theta_{\text{Smax}})$  of single dimers.

**FIG. 6 (a)** FDTD calculation setup for electric fields around a single NP dimer by

wide-field excitation from the upper side with respect to the coordinate system. Polarization directions of the excitation light are indicated by gray arrows. **(b)** Dimer composed of two NP with diameters of  $D_1$  and  $D_2$ , respectively. The gap was set to 1 nm. The position of the HS is indicated by the red dot **(c)**  $\sigma_{\text{sca}}(\omega)$  spectrum (blue curve) and  $\sigma_{\text{abs}}(\omega)$  spectrum (green curve) of a dimer with  $D_1$  and  $D_2$  of 35 nm with the incident light polarized with respect to the x-axis. **(d)**  $F_{\text{R}}(\omega)$  spectrum (red curve) of a dimer with  $D_1$  and  $D_2$  of 35 nm with incident light polarized with respect to the x-axis with a phase of  $E_{\text{loc}}$  (black curve) at the center gap, indicated by the red dot in **(b)**.

**FIG. 7 (a1)–(a10)**  $\sigma_{\text{sca}}(\omega)$  spectra of single NPs with diameters of 30, 35, 40, 50, 60, 80, 100, 120, and 140 nm, respectively. D, Q, and H indicate dipole, quadrupole, and hexapole resonance, respectively. **(b1)** and **(b2)** Dipole and quadrupole on single NPs raised by light coming along the y axis. **(c1)** and **(c2)** Dipole and quadrupole coupled resonance for symmetric and asymmetric dimers, respectively.

**FIG. 8 (a1)–(a6)**  $\sigma_{\text{sca}}(\omega)$  spectra (blue lines) and  $F_{\text{R}}(\omega)$  spectra (red lines) of single symmetric dimers with diameters of 30, 40, 60, 80, 100, and 120 nm, respectively.

**(b1)–(b6)**  $\sigma_{\text{sca}}(\omega)$  spectra (blue lines) and  $F_{\text{R}}(\omega)$  spectra (red lines) of single asymmetric

dimers with a  $D_1$  of 30 nm and  $D_2$  of 30, 50, 80, 100, 120, and 140 nm, respectively.

**FIG. 9 (a1)–(a4)**  $D_1$  dependence of the  $\sigma_{\text{sca}}(\omega)$  and  $\sigma_{\text{abs}}(\omega)$  spectra with the phases of  $E_{\text{loc}}$  with a  $D_1$  of 30 nm and  $D_2$  of 30, 50, 80, and 120 nm, respectively. The initial phase of  $E_1$  and  $D_2$  were set  $180^\circ$  and 30 nm, respectively. **(b1)–(b4)**  $D_1$  dependence of the  $F_{\text{R}}(\omega)$  spectra and the phases of  $E_{\text{loc}}$  with a  $D_1$  of 30 nm and  $D_2$  of 30, 50, 80, and 120 nm, respectively. The initial phase of  $E_1$  and  $D_2$  were set  $180^\circ$  and 30 nm, respectively. **(c1)–(c4)**  $D_1$  dependence of the  $\sigma_{\text{abs}}(\omega)$  and  $F_{\text{R}}(\omega)$  spectra with a  $D_1$  of 30 nm and  $D_2$  of 30, 50, 80, and 120 nm, respectively.

**FIG. 10 (a1)–10(a4)** NP diameter dependences of the spectra of  $\sigma_{\text{sca}}(\omega)$  **(a1)**,  $\sigma_{\text{abs}}(\omega)$  **(a2)**, and  $F_{\text{R}}(\omega)$  **(a3)** as well as the phase of  $E_{\text{loc}}$  **(a4)** at HSs for symmetric dimers, expressed as contour maps. The black circles and triangles indicate the phase retardations of  $E_{\text{loc}}$  for  $90^\circ$  and  $180^\circ$ , respectively, at HSs in Fig. 6(b). **(b1)–10(b4)**  $D_1$  dependences of spectra of  $\sigma_{\text{sca}}(\omega)$  **(b1)**,  $\sigma_{\text{abs}}(\omega)$  **(b2)**,  $F_{\text{R}}(\omega)$  **(b3)** as well as the phase of  $E_{\text{loc}}$  **(b4)** at HSs for asymmetric dimers while fixing  $D_2$  at 30 nm, expressed as contour maps. The black circles and triangles indicate the phase retardations of  $E_{\text{loc}}$  for  $90^\circ$  and  $180^\circ$ , respectively, at HSs in Fig. 6(b). The higher energy regions in **(a4)** and **(b4)** are

sealed to avoid complex phase inversion.

**FIG. 11 (a)** Calculated relationship between  $\hbar\omega_p$  and  $\hbar\omega_F$  of single symmetric dimers ( $\circ$ ) and asymmetric dimers with  $D_2$  values of 30 ( $\square$ ), 35 ( $\triangle$ ), 40 ( $\nabla$ ), 60 ( $\diamond$ ) nm. The diameters of the NP symmetric dimers are 30–140 nm.  $D_1$  values for the asymmetric dimers are 30–140 ( $\square$ ), 35–140 ( $\triangle$ ), 40–140 ( $\nabla$ ), and 60–140 ( $\diamond$ ) nm. The experimental relationship between  $\hbar\omega_p$  and  $\hbar\omega_S$  of single dimers ( $\circ$ ) taken from [Fig. 3\(a\)](#). **(b)** Calculated relationship between  $\hbar\omega_d$  and  $\hbar\omega_F$  of single symmetric dimers ( $\circ$ ) and asymmetric dimers with  $D_2$  values of 30 ( $\square$ ), 35 ( $\triangle$ ), 40 ( $\nabla$ ), and 60 ( $\diamond$ ) nm. The diameters of the NP symmetric dimers are 30–140 nm.  $D_1$  values for the asymmetric dimers are 30–140 ( $\square$ ), 35–140 ( $\triangle$ ), 40–140 ( $\nabla$ ), and 60–140 ( $\diamond$ ) nm, respectively. The experimental relationship between  $\hbar\omega_d$  and  $\hbar\omega_S$  of single dimers ( $\circ$ ) taken from [Fig. 3\(b\)](#). **(c)** Calculated relationship between  $\hbar\omega_p$  and  $\sigma_{\text{sca}}(\omega_p)$  of single symmetric dimers ( $\circ$ ) and asymmetric dimers with  $D_2$  values of 30 ( $\square$ ), 35 ( $\triangle$ ), 40 ( $\nabla$ ), and 60 ( $\diamond$ ) nm. The diameters of the NP symmetric dimers are 30–140 nm.  $D_1$  values for the asymmetric dimers are 30–140 ( $\square$ ), 35–140 ( $\triangle$ ), 40–140 ( $\nabla$ ), 60–140 ( $\diamond$ ) nm, respectively. The experimental relationship between  $\hbar\omega_p$  and  $\sigma_{\text{sca}}(\omega_p)$  of single dimers ( $\circ$ ) from [Fig. 3\(c\)](#).

FIG. 12 (a1)–10(a4) Polarization dependence of  $\sigma_{\text{sca}}(\omega)$  spectra with  $D_1$  of 30 nm and  $D_2$  of 30 (a1), 50 (a2), 80 (a3), and 120 (a4) nm, respectively, with excitation polarization parallel (solid blue curves) and perpendicular (dashed blue curves) to the dimer long axis. (b1)–10(b4) Polarization dependence of  $F_{\text{R}}(\omega)$  spectra with  $D_1$  values of 30 nm and  $D_2$  values of 30 (b1), 50 (b2), 80 (b3), and 120 (b4) nm, with excitation polarization parallel (solid red curves) and perpendicular (dashed red curves) to the dimer long axis. (c1)–10(c4) Polarization angle dependence of  $\sigma_{\text{sca}}(\omega)$  spectra with  $D_1$  of 30 nm and  $D_2$  of 30 (c1), 50 (c2), 80 (c3), and 120 (c4) nm, expressed as contour maps. The spectral maxima and dips are indicated by solid and dashed circles, respectively. (d1)–10(d4) Polarization angle dependence of  $\sigma_{\text{sca}}(\omega_{\text{p}})$  (blue curves) and  $F_{\text{R}}(\omega_{\text{F}})$  (red points) with  $D_1$  of 30 nm and  $D_2$  of 30 (d1), 50 (d2), 80 (d3), and 120 (d4) nm.

FIG. 13 Calculated relationship between  $\theta_{\text{Pmax}} - \theta_{\text{FMax}}$  and  $\hbar\omega_{\text{P}} - \hbar\omega_{\text{F}}$  of single dimers, where  $\theta_{\text{Fmax}}$  is the polarization angle that maximizes  $F_{\text{R}}(\omega_{\text{F}})$ . The experimental relationship between  $\theta_{\text{Pmax}} - \theta_{\text{SMax}}$  and  $\hbar\omega_{\text{P}} - \hbar\omega_{\text{S}}$  of single dimers. The calculated relationship of single symmetric dimers ( $\circ$ ) and asymmetric dimers with  $D_2$  values of 30 ( $\square$ ), 35 ( $\Delta$ ), 40 ( $\nabla$ ), and 60 ( $\diamond$ ) nm. The diameters of NP symmetric dimers are

30–140 nm.  $D_1$  values for asymmetric dimers are 30–140 ( $\square$ ), 35–140 ( $\Delta$ ), 40–140 ( $\nabla$ ), and 60–140 ( $\diamond$ ) nm, respectively. The experimental relationship of single dimers ( $\circ$ ) from Fig. 5(a).

**FIG. 14** (a) Normalized  $\sigma_{\text{sca}}(\omega)$  and  $F_{\text{R}}(\omega)$  spectra with the phases of  $E_{\text{loc}}$  at the HS of a dimer with  $D_1$  of 35 nm and  $D_2$  of 100 nm. The initial phase of  $E_1$  is set  $180^\circ$ . The three vertical solid lines indicate the positions for the phase retardation of  $90^\circ$ ,  $180^\circ$ , and  $270^\circ$ . (b1)–(b3) Schematic images of charge distributions of the z plane of a dimer for DD, DQ, and DD coupled resonance at the three spectral positions in (a). (c) Polar diagrams of the radiation patterns of the z plane for quadrupole, dipole, and DQ coupled resonance. The blue arrows indicate the directions of the electric fields. (d1)–(d3) Distributions of the  $E_{\text{loc}}$  of the y plane of a dimer for DD, DQ, and DD coupled plasmons at the three spectral positions in (a). (e1)–(e3) Polar diagram of the radiation patterns at the three spectral positions in (a).

**FIG. 15** Definition of  $\phi$  of the radiation patterns in the polar diagram. Relationships between the  $D_1/D_2$  and  $\phi$  of single symmetric dimers ( $\circ$ ) and asymmetric dimers with  $D_2$  values of 30 ( $\square$ ), 35 ( $\Delta$ ), 40 ( $\nabla$ ), and 60 ( $\diamond$ ) nm. The diameters of the NP symmetric

dimers are 30–140 nm.  $D_1$  values for the asymmetric dimers are 30–140 ( $\square$ ), 35–140 ( $\Delta$ ), 40–140 ( $\nabla$ ), and 60–140 ( $\diamond$ ) nm, respectively. The arrow indicates the trend of Type I or II dimers.

FIG. 1

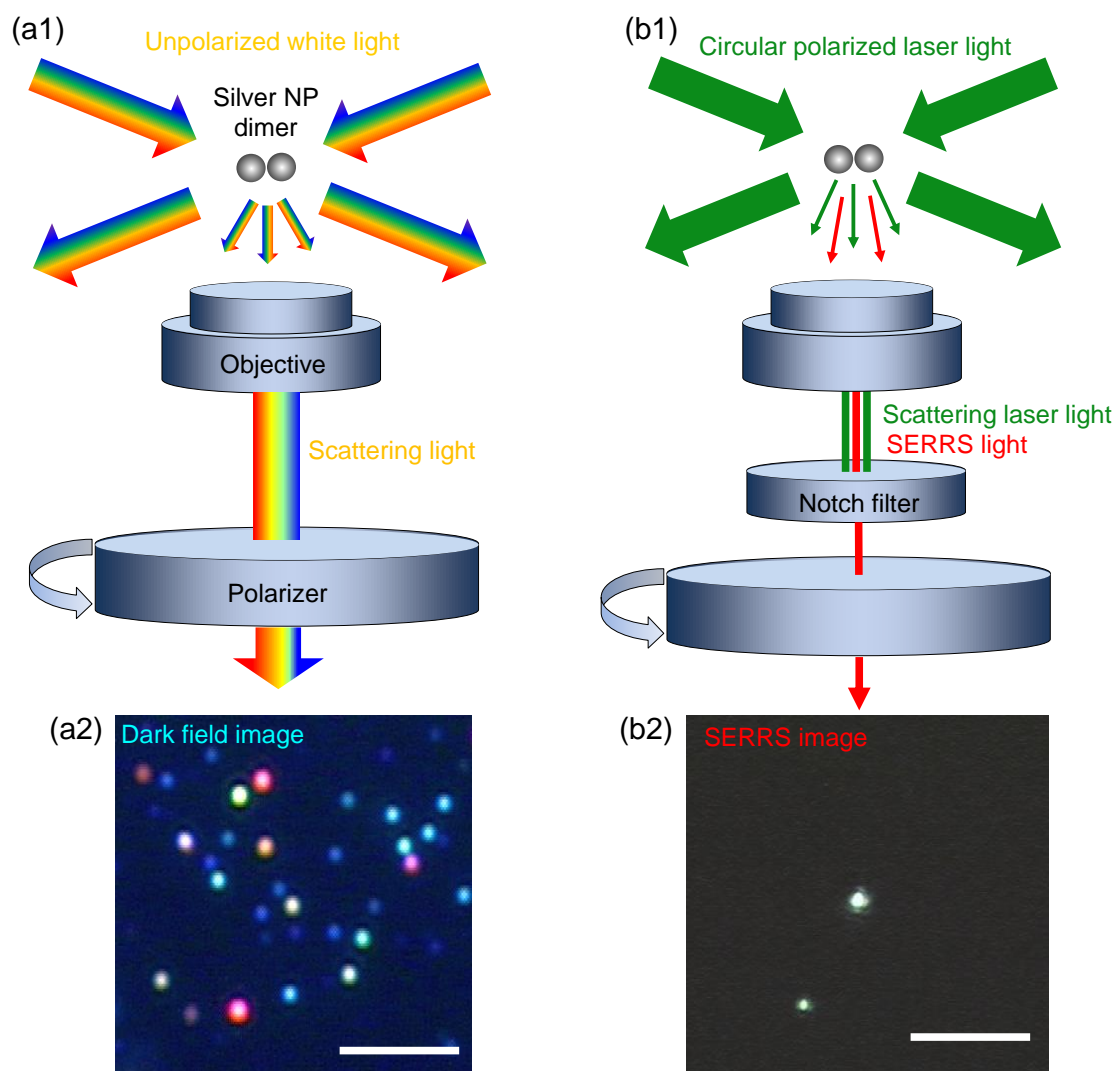


FIG. 2

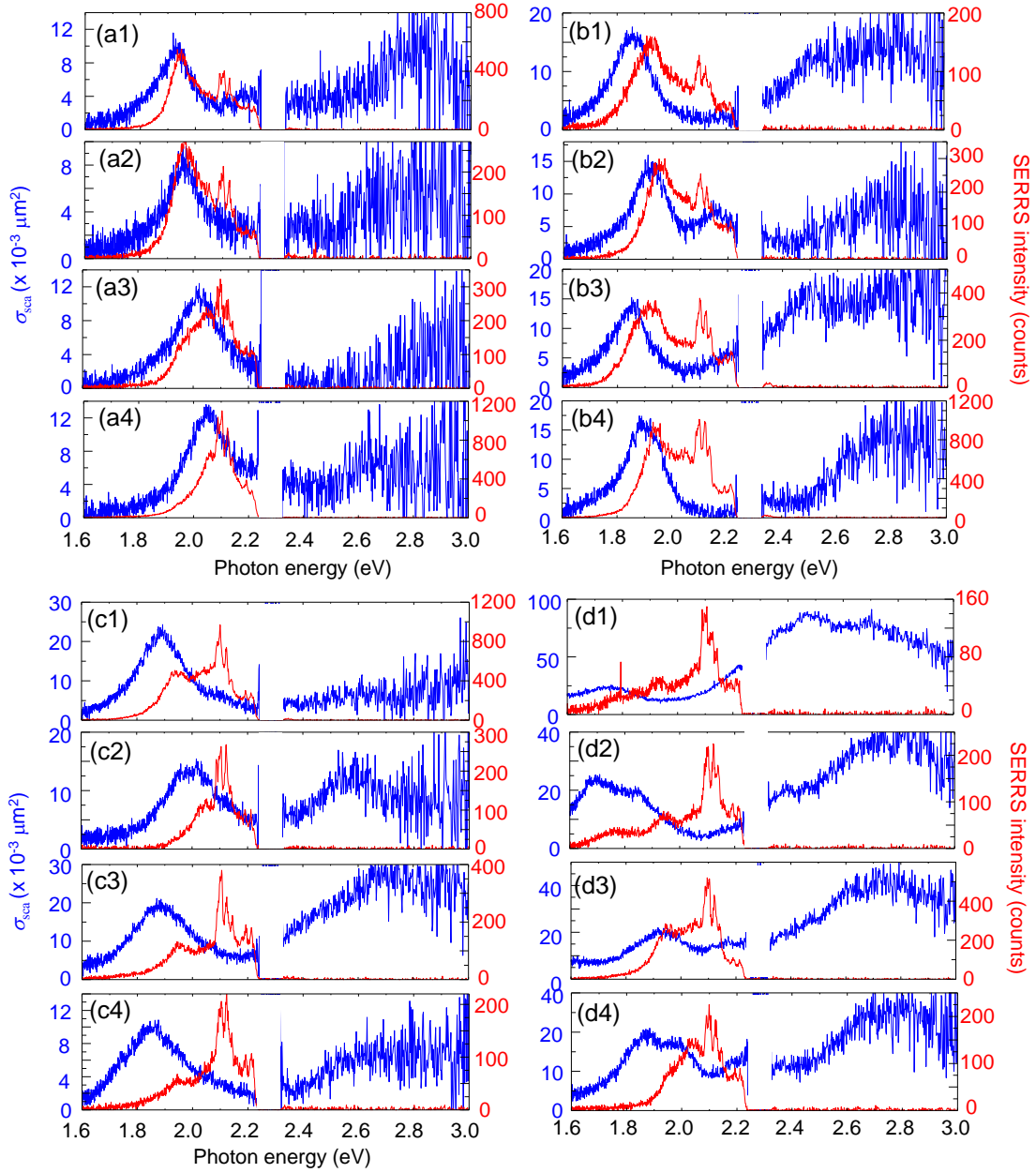


FIG. 3

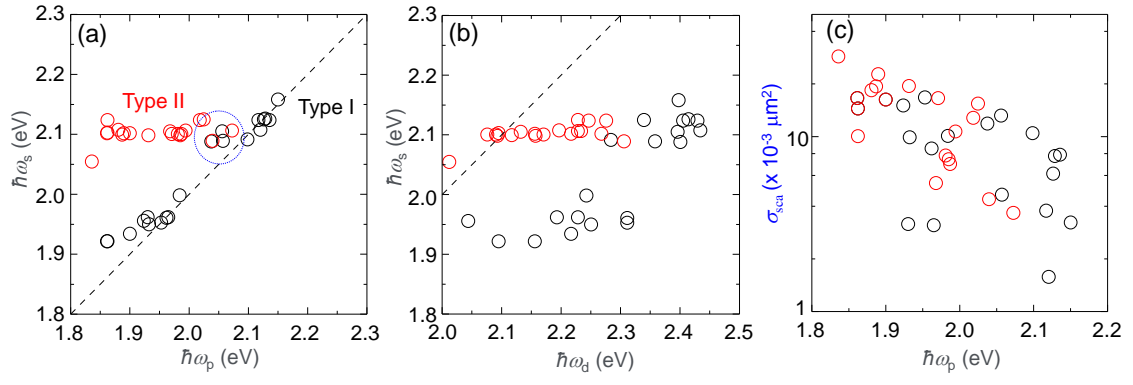


FIG. 4

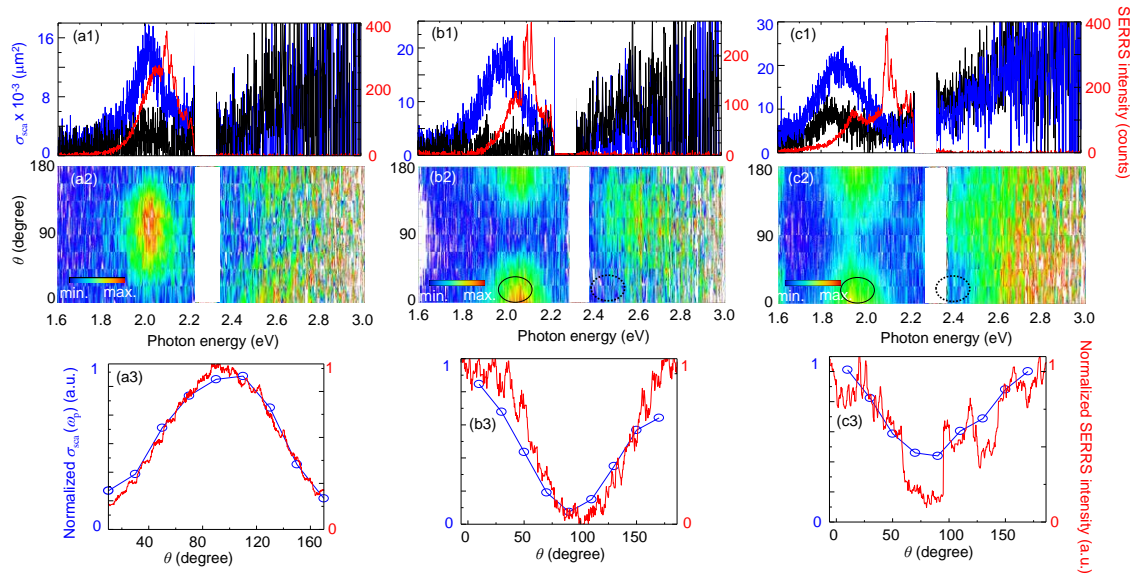


FIG. 5

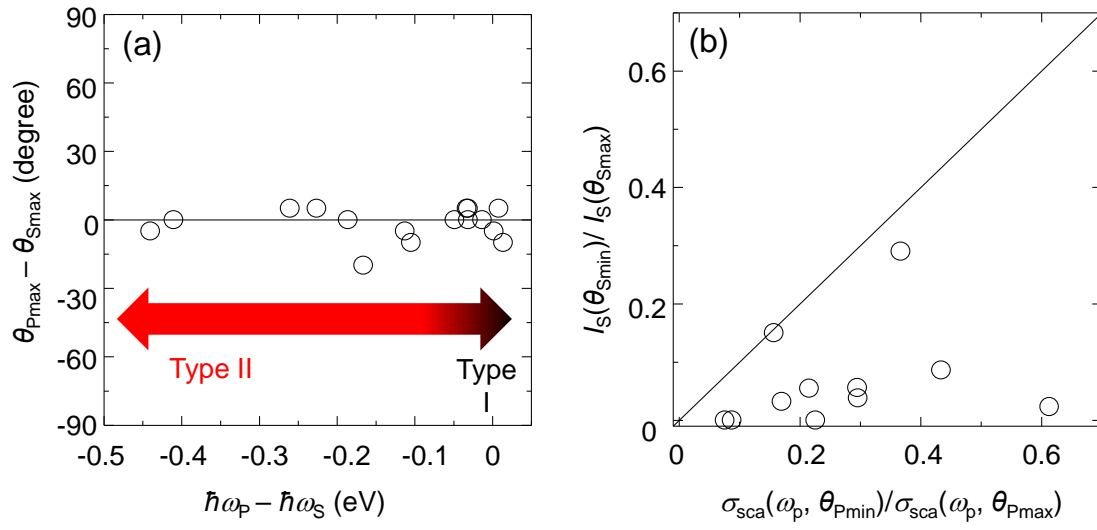


FIG. 6

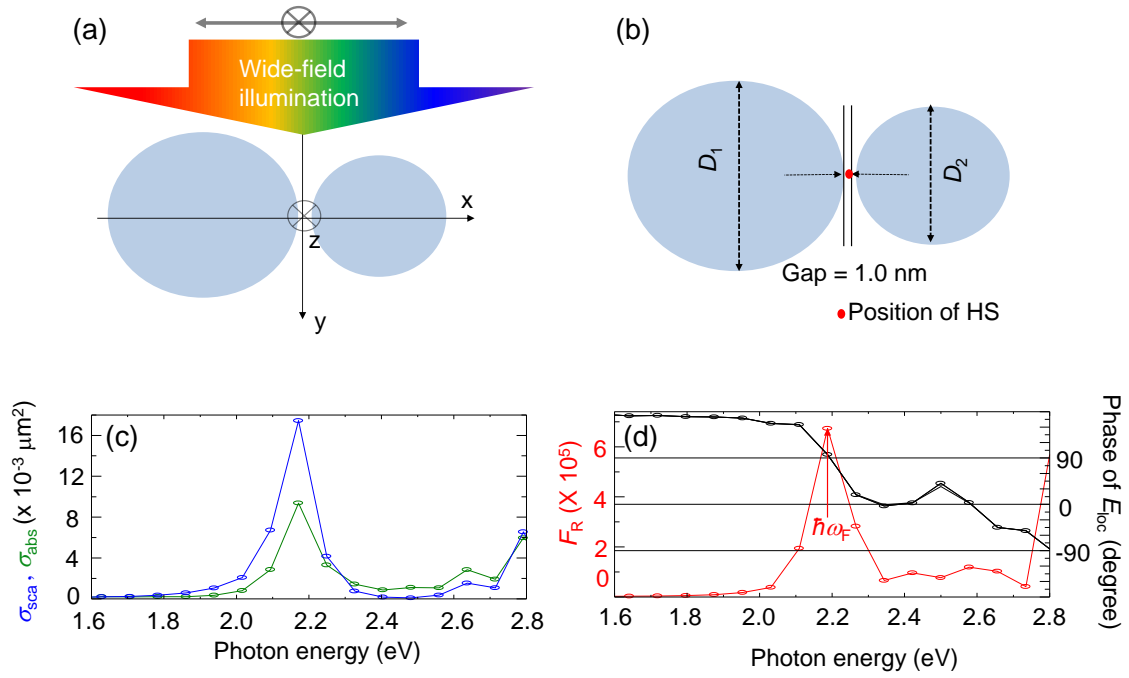


FIG. 7

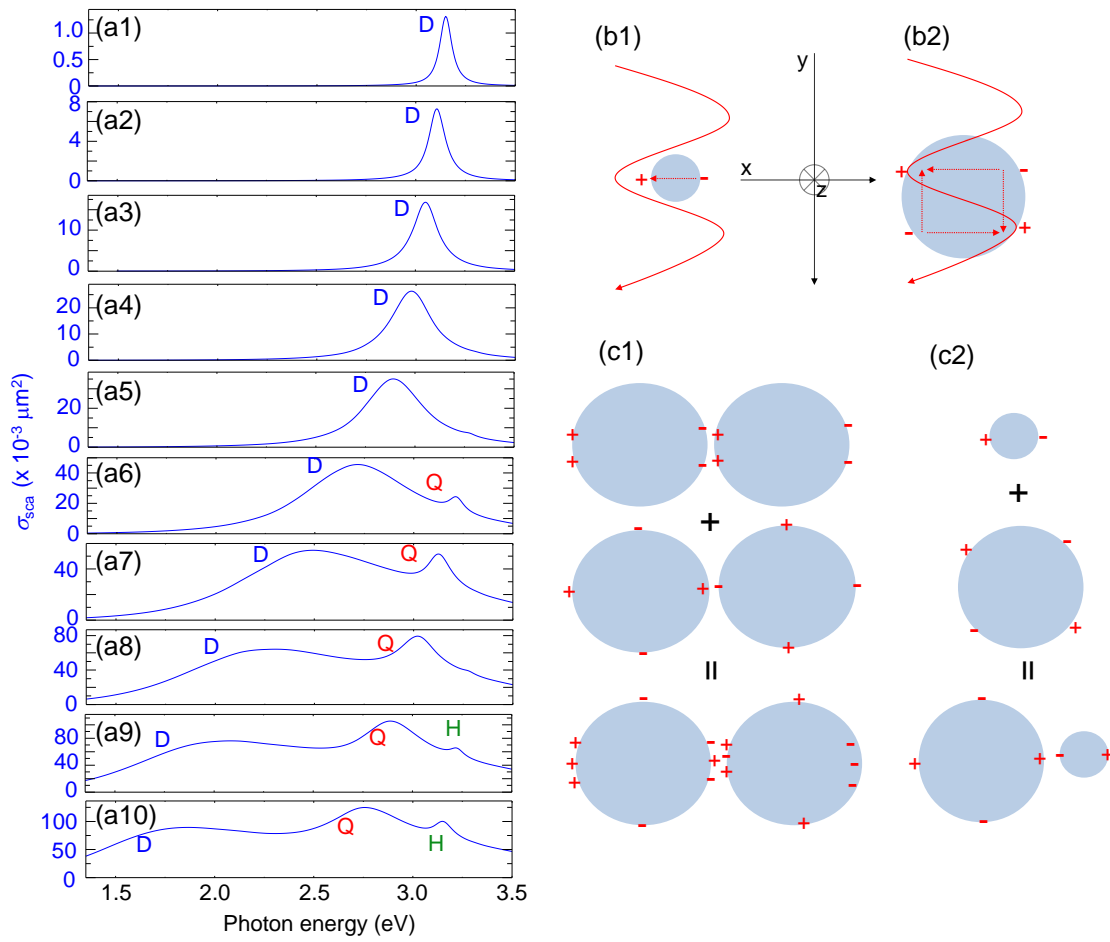


FIG. 8

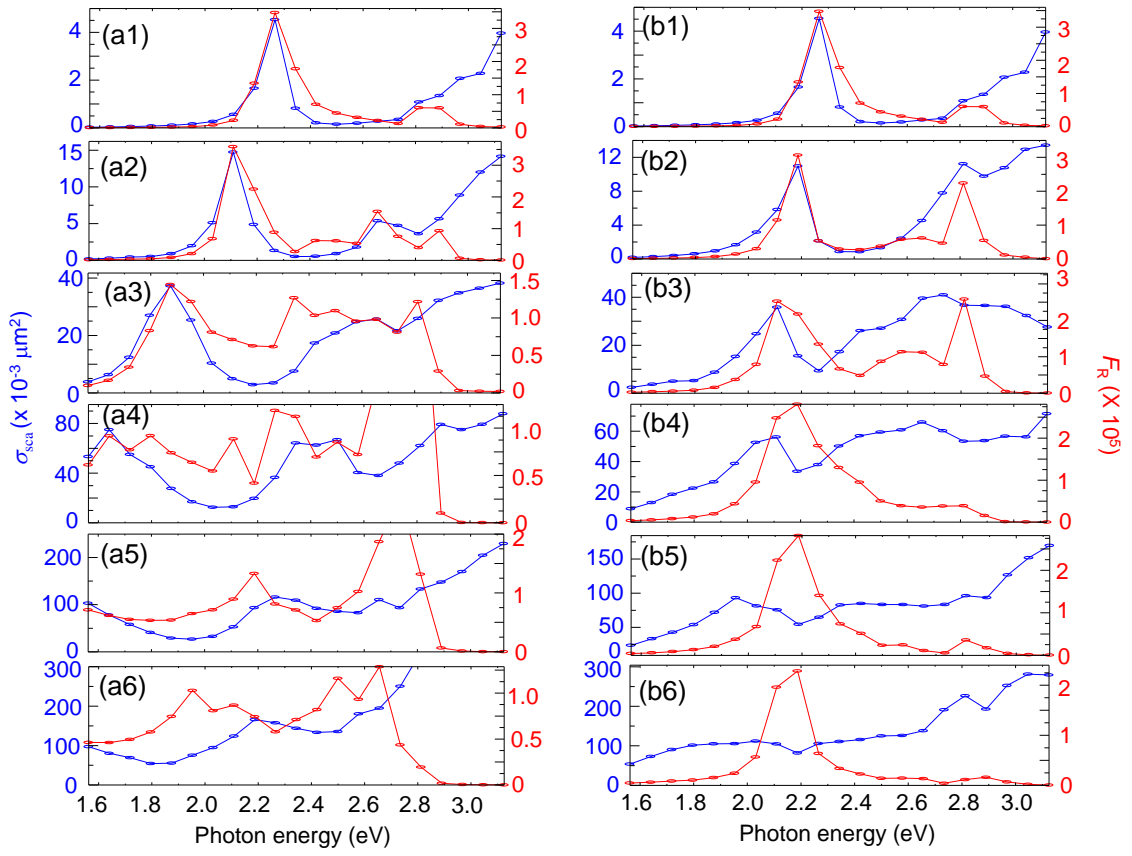


FIG. 9

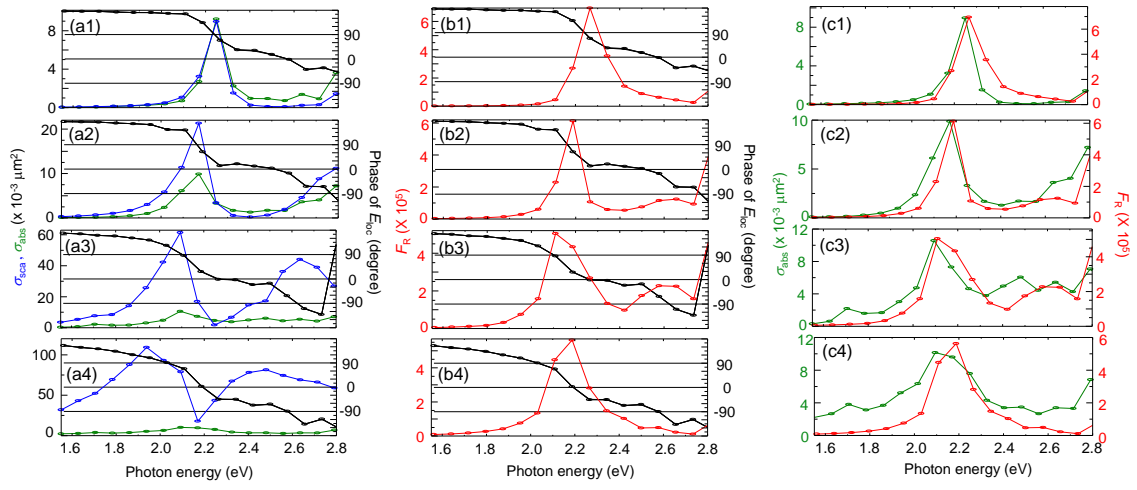


FIG. 10

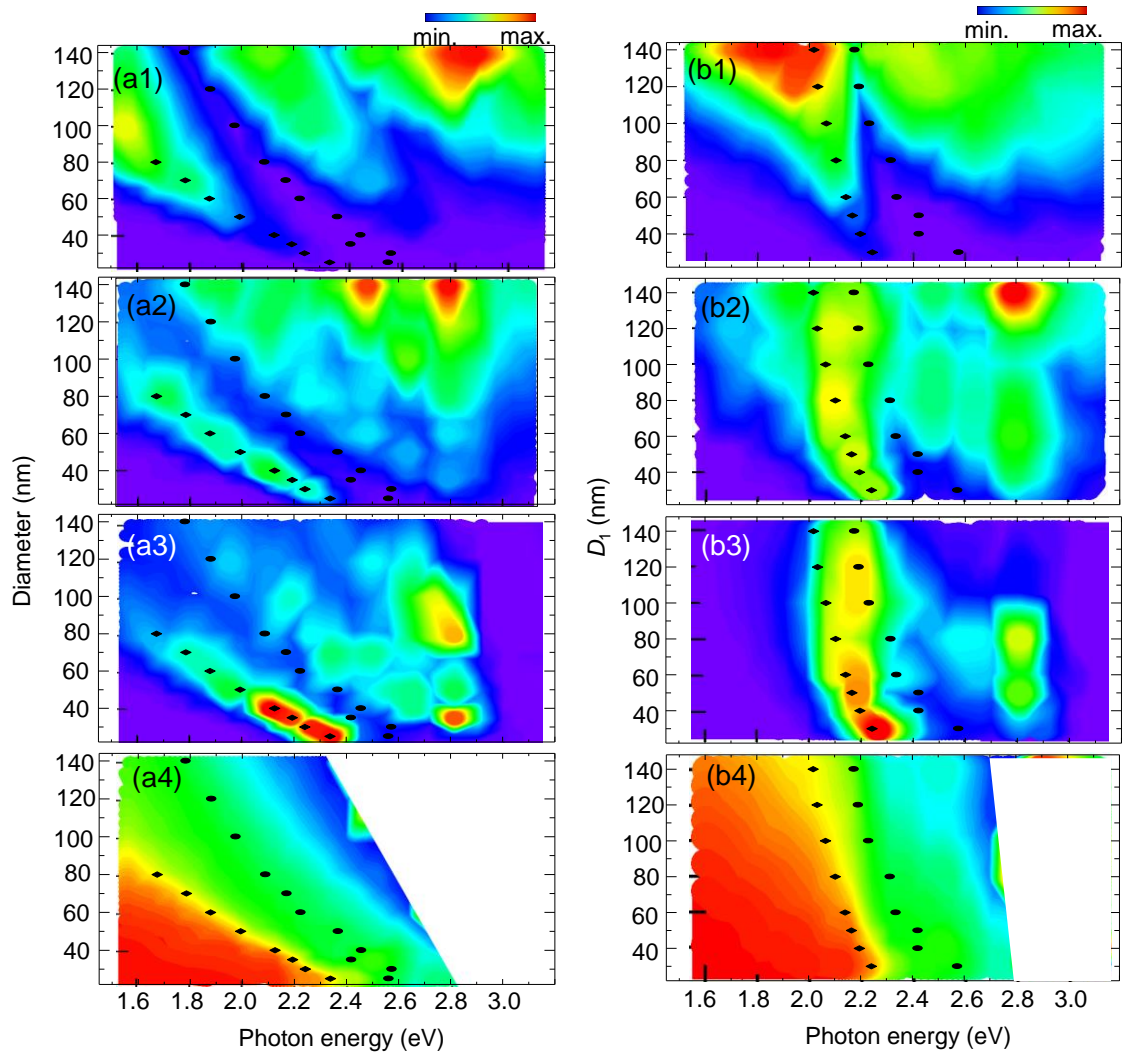


FIG. 11

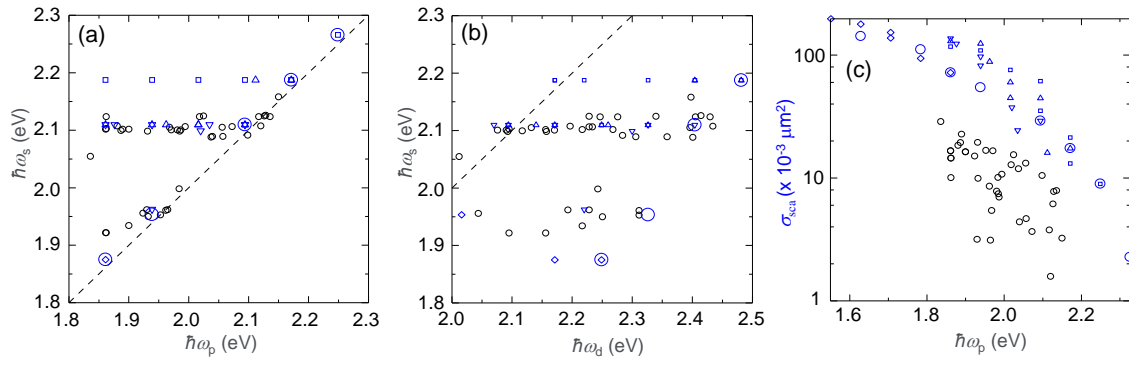


FIG. 12

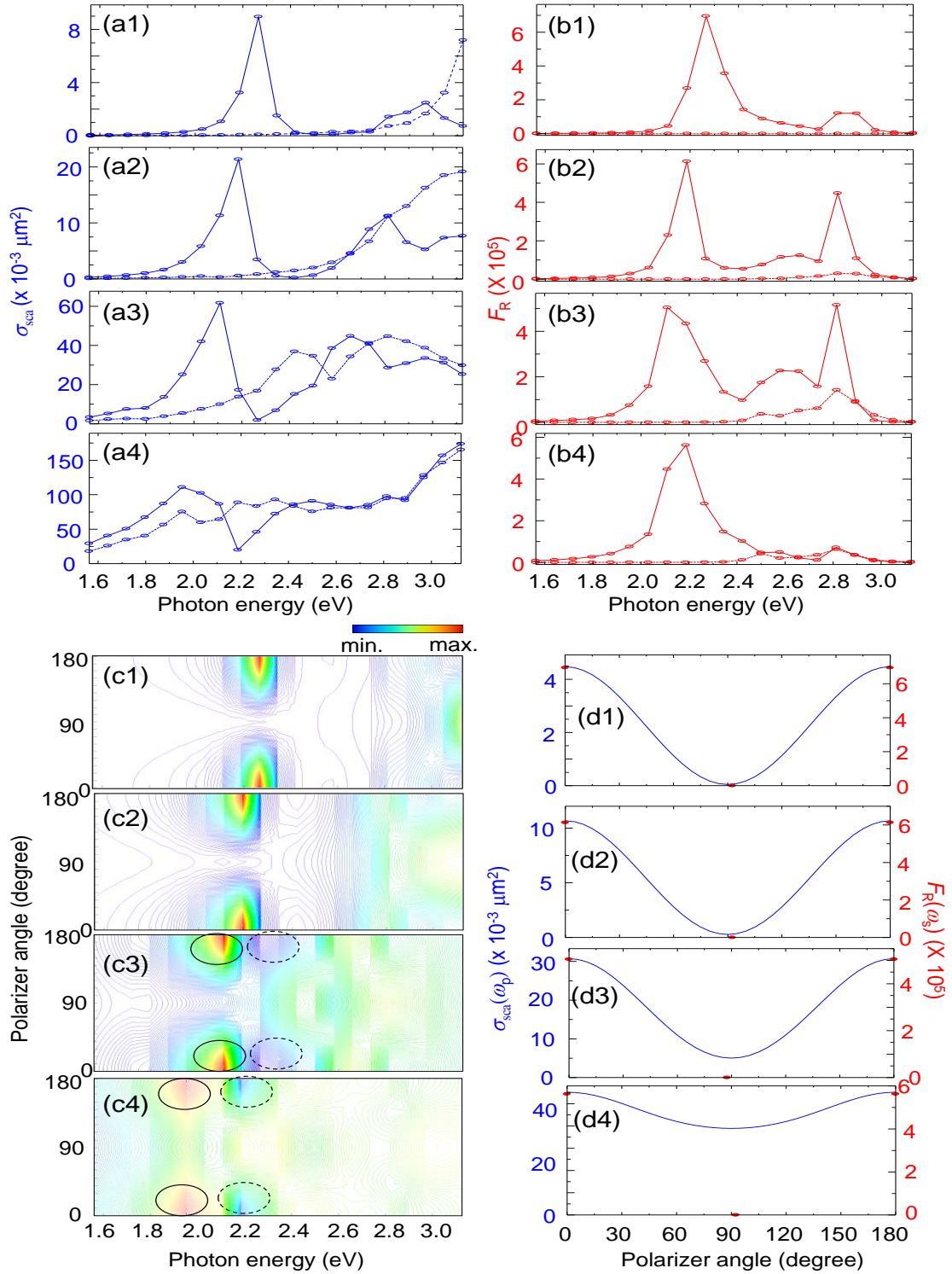


FIG. 13

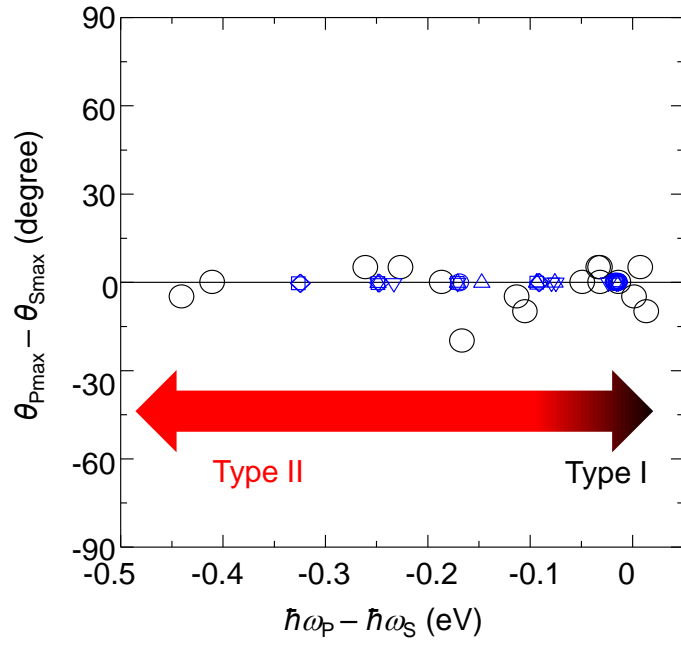


FIG. 14

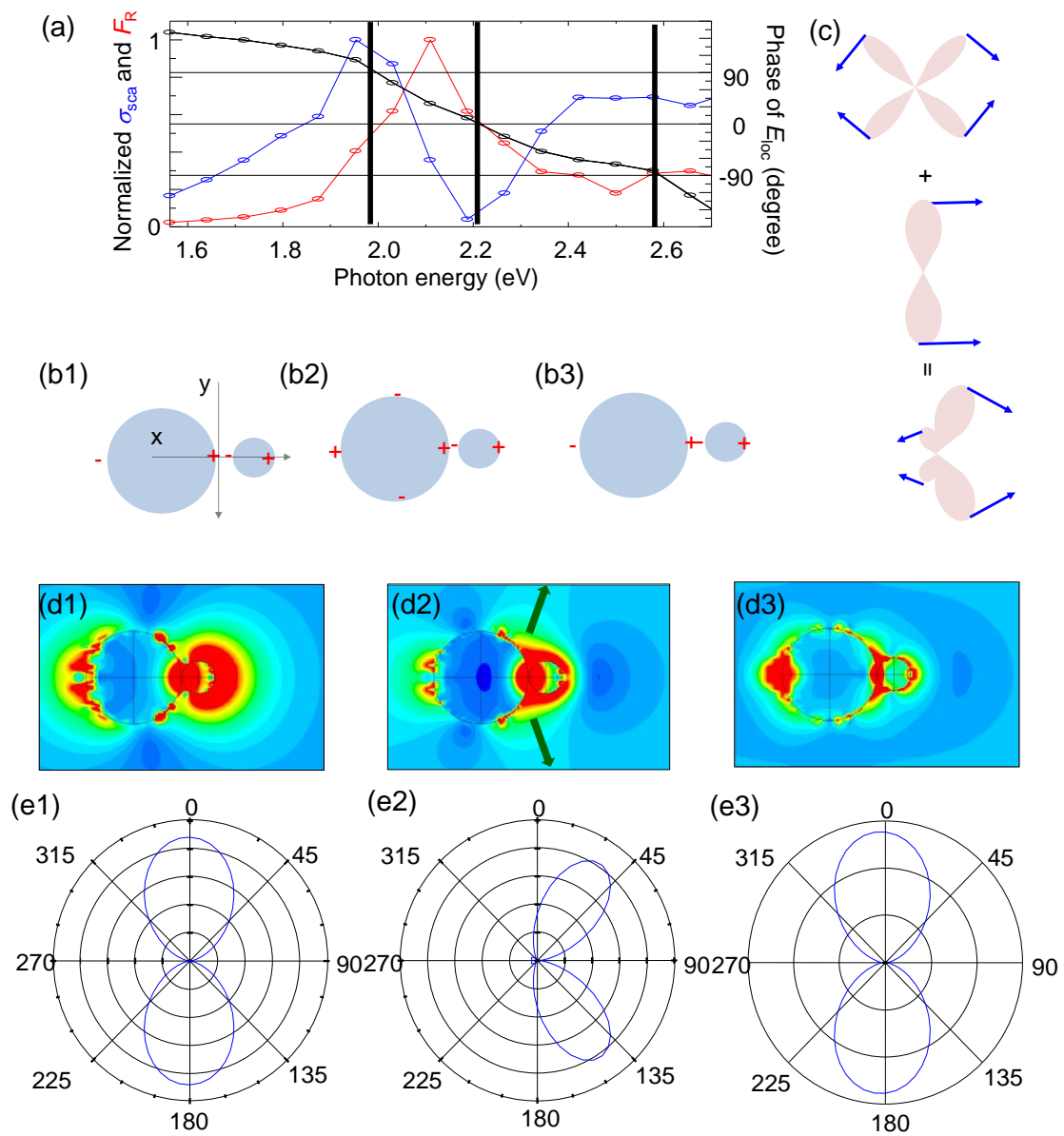


FIG. 15

